

# EVOLUTION OF THE COOL GAS IN THE CIRCUMGALACTIC MEDIUM (CGM) OF MASSIVE HALOS – A KECK COSMIC WEB IMAGER (KCWI) SURVEY OF LY $\alpha$ EMISSION AROUND QSOs AT $Z \approx 2$

ZHENG CAI<sup>1,2</sup>; SEBASTIANO CANTALUPO<sup>3</sup>; J. XAVIER PROCHASKA<sup>2,4</sup>; FABRIZIO ARRIGONI BATTALIA<sup>5</sup>; JOE BURCHETT<sup>2</sup>;  
QIONG LI<sup>6</sup>; JOHN CHISHOLM<sup>2</sup>; KEVIN BUNDY<sup>2</sup>; JOSEPH F. HENNAWI<sup>7</sup>

<sup>1</sup> Department of Astronomy, Tsinghua University, Beijing 100084, China

<sup>2</sup> UCO/Lick Observatory, University of California, 1156 High Street, Santa Cruz, CA 95064, USA

<sup>3</sup> Department of Physics, ETH Zurich, Wolfgang-Pauli-Strasse 27, CH-8093 Zurich, Switzerland

<sup>4</sup> Kavli Institute for the Physics and Mathematics of the Universe (WPI), The University of Tokyo, Kashiwa 277-8583, Japan

<sup>5</sup> Max-Planck Institut für Astrophysik, Karl-Schwarzschild-Strasse 1, 85748 Garching, Germany

<sup>6</sup> Kavli Institute for Astronomy and Astrophysics, Peking University, Beijing 100871, China and

<sup>7</sup> Department of Physics, Broida Hall, University of California at Santa Barbara, Santa Barbara, CA 93106, USA

*Accepted to AAS Journals*

## ABSTRACT

Motivated by the recent discovery of the near-ubiquity of Ly $\alpha$  emission around  $z \gtrsim 3$  QSOs, we performed a systematic study of QSO circumgalactic Ly $\alpha$  emission at  $z \approx 2$ , utilizing the unique capability of the Keck Cosmic Web Imager (KCWI) – a new wide-field, blue sensitive integral-field spectrograph (IFU). In this paper, we present KCWI observations on a sample of 16 ultraluminous Type-I QSOs at  $z = 2.1 - 2.3$  with ionizing luminosities of  $L_{\nu_{\text{LL}}} = 10^{31.1-32.3} \text{ erg s}^{-1} \text{ Hz}^{-1}$ . We found that 14 out of 16 QSOs are associated with Ly $\alpha$  nebulae with projected linear-sizes larger than 50 physical kpc (pkpc). Among them, four nebulae have enormous Ly $\alpha$  emission with the Ly $\alpha$  surface brightness  $SB_{\text{Ly}\alpha} > 10^{-17} \text{ erg s}^{-1} \text{ cm}^{-2} \text{ arcsec}^{-2}$  on the  $> 100$  kpc scale, extending beyond the field of view of KCWI. Our KCWI observations reveal that most  $z \approx 2$  QSO nebulae have a more irregular morphology compared to those at  $z \gtrsim 3$ . In turn, we measure that the circularly-averaged surface brightness (SB) at  $z \approx 2$  is 0.4 dex fainter than the redshift-corrected, median SB at  $z \gtrsim 3$ . The Ly $\alpha$  SB profile ( $SB_{\text{Ly}\alpha}$ ) of QSOs at  $z \approx 2$  can be described by a power law of  $SB_{\text{Ly}\alpha, z \approx 2.3} = 3.7 \times 10^{-17} \times (r/40)^{-1.8} \text{ erg s}^{-1} \text{ cm}^{-2} \text{ arcsec}^{-2}$ , with the slope similar to that at  $z \gtrsim 3$ . The observed lower redshift-corrected, circularly-averaged SB may be mainly due to the lower covering factor of cool gas clouds in massive halos at  $z \approx 2$ .

*Subject headings:* Intergalactic medium, QSOs: emission lines, galaxy: halos

## 1. INTRODUCTION

Over the past decade, theoretical studies have established a new paradigm for the accretion of gas into dark matter halos to fuel star-formation during galaxy formation (e.g., Dekel et al. 2009; Kereš et al. 2009; Nelson et al. 2013; Vogelsberger et al. 2013). This model predicts that galaxies are fed by cool ‘streams’ of gas, linked to the surrounding intergalactic medium (IGM) by a web of cosmic filaments (e.g., Bond et al. 1996; Fukugita et al. 1998). These filaments contain a rich reservoir of nearly pristine gas that drives galaxy formation and evolution, especially in the early Universe (e.g., Kereš et al. 2005; Dekel et al. 2009; van de Voort et al. 2011; Fumagalli et al. 2011; Dekel et al. 2013; Correa et al. 2015). Nevertheless, this fundamental picture is difficult to test observationally. Direct imaging of the IGM is crucial for examining this standard paradigm of galaxy formation and further revealing the IGM-galaxy interactions.

The detection of the IGM in emission was suggested a few decades ago (e.g., Hogan & Weymann 1987; Gould & Weinberg 1996). Nevertheless, progress was hindered by the faintness of the IGM emission. By searching around luminous QSOs, the expected diffuse emission due to recombination should be enhanced by a few orders of magnitude within the densest part of the cosmic web (e.g., Cantalupo et al. 2005, 2012; Kollmeier et al. 2010). With narrowband imaging, Cantalupo et al. (2014); Hennawi et al. (2015) and Cai et al. (2017) discovered a few sources

that are sufficiently luminous for quantitative analysis of diffuse gas emission. These sources define the “Enormous Ly $\alpha$  Nebulae (ELANe)” (e.g., Cai et al. 2017; Arrigoni Battaia et al. 2018; Cai et al. 2018; Arrigoni Battaia et al. 2019); they are the extrema of Ly $\alpha$  nebulosities at  $z \sim 2 - 3$ , with sizes exceeding the diameters of massive dark matter halos ( $\sim 200$  kpc) with  $SB_{\text{Ly}\alpha} \geq 10^{-17} \text{ erg s}^{-1} \text{ cm}^{-2} \text{ arcsec}^{-2}$  and Ly $\alpha$  luminosities greater than  $10^{44} \text{ erg s}^{-1}$ .

Recent progress in wide-field integral-field spectrographs (IFS) on 8-10m telescopes, including MUSE and KCWI, provide us an indispensable opportunity to directly study the IGM/CGM around bright sources at  $z = 2 - 4$  by reaching an unprecedented, low surface brightness (SB) of a few  $\times 10^{-19} \text{ erg s}^{-1} \text{ cm}^{-2} \text{ arcsec}^{-2}$ . This makes it possible to study emission from the circumgalactic medium (CGM) and IGM around bright sources. With VLT/MUSE and using a sample of 17 QSOs, Borisova et al. (2016) reveal that Ly $\alpha$  nebulae with projected sizes exceeding 100 kpc are ubiquitous for QSOs at  $z \gtrsim 3$ . Arrigoni Battaia et al. (2019) further confirmed such near-ubiquity using a sample of 61 QSOs at  $z \gtrsim 3$ . Nevertheless, a systematic IFS survey has not been performed at  $z < 3$ . A crucial question is whether one can construct a uniform sample at a lower redshift (e.g., at  $z \sim 2$ ), and probe evolution in the IGM/CGM across cosmic time.

At  $z \approx 2$ , Arrigoni Battaia et al. (2016) have conducted

deep narrowband images on 15  $z \approx 2.2$  QSOs which have a fainter luminosity compared with QSO sample at  $z \gtrsim 3$  (Borisova et al. 2016; Arrigoni Battaia et al. 2019). Arrigoni Battaia et al. (2016) did not detect bright nebulae with the projected size of  $> 50$  kpc at Ly $\alpha$  SB of  $10^{-17}$  erg s $^{-1}$  cm $^{-2}$  arcsec $^{-2}$ . Compared with the ubiquitous Ly $\alpha$  nebulae at  $z \approx 3$ , the narrowband results seem to suggest a strong evolution of Ly $\alpha$  emitting cool gas from  $z = 3$  to  $z = 2$ . However, before drawing such a conclusion, we note that the following effects may partially yield such a low detection rate of Ly $\alpha$  nebulae at  $z \approx 2$  (also see §4.1.3 in Arrigoni Battaia et al. 2019): (1) The redshift of nebular Ly $\alpha$  may have an offset with the systemic redshift determined by the Mg II emission. If we use a narrowband with the central wavelength consistent with the Mg II-determined systemic redshift, then the Ly $\alpha$  emission could reside outside the narrowband; (2) The full-width-half-maximum (FWHM) of the narrowband is still much wider than the FWHM of the nebular Ly $\alpha$  emission. Thus, the contrast between the point-spread-function (PSF) and the diffuse Ly $\alpha$  emission is higher for the narrowband data comparing to the IFU data, which makes the PSF subtraction more difficult for the narrowband data. (3) The surface brightness limit that MUSE reaches is deeper than the narrowband study which may also yield a higher detection rate of the Ly $\alpha$  nebulae.

To build a uniform sample for studying IGM emission at  $z \approx 2$  and directly test its evolution, we have conducted a new survey using the Keck Cosmic Web Imager (KCWI) to search for Ly $\alpha$  nebulae associated with QSOs at  $z \approx 2$ . With the KCWI, we can conduct, for the first time, a fair comparison with  $z \gtrsim 3$  MUSE results, by selecting QSOs with similar ionizing luminosities as that of the MUSE samples (Borisova et al. 2016; Arrigoni Battaia et al. 2019). Our goals are to understand the cool gas budget around ultraluminous QSOs at  $z \approx 2$ , to study the kinematics throughout QSO halos, and to probe the evolution of the CGM around massive halos from  $z = 3 - 2$ .

In this paper, we present the first KCWI observations on the Ly $\alpha$  nebulae associated with ultraluminous Type-I QSOs at  $z = 2.1 - 2.3$ . We organize this paper as follows. In §2, we introduce our observations and data reduction. In §3, we provide the results of the KCWI observations, perform optimal extraction of Ly $\alpha$  emission around QSOs, and study the gas kinematics and morphology. In §4, we provide a discussion of the results. The discussion is based on the observational results from the KCWI, MUSE, and previous narrowband studies. Throughout this paper when measuring distances, we refer to physical distances unless otherwise specified. We assume a  $\Lambda$ CDM cosmology with  $\Omega_m = 0.3$ ,  $\Omega_\Lambda = 0.7$  and  $h = 0.70$ .

## 2. OBSERVATIONS

In this section, we provide details on the KCWI instrument configurations, observations, data reduction pipeline, and post-processing after the standard reduction pipeline.

### 2.1. KCWI Instrument Configuration

Keck Cosmic Web Imager (KCWI) (e.g., Morrissey et al. 2018) is a general purpose, optical IFS that has been

installed on the 10 m Keck II telescope. KCWI provides seeing-limited imaging from the wavelength range of 3500 – 5700 Å, and the spectral resolution can be configured from  $R = 1000$  to  $R = 20000$ . The field of view is  $20'' \times 33''$  for large slicer,  $16'' \times 20''$  for the medium slicer and  $8'' \times 20''$  for the small slicer. KCWI is optimal for a survey of gaseous nebulae at  $z \approx 2$  because: (1) KCWI has a high throughput from  $\lambda = 3800 - 5500\text{\AA}$ , optimal for probing the Ly $\alpha$ , C IV, and He II lines at  $z \sim 2$ . (2) KCWI has high spectral-resolution modes ( $R > 4000$ ) which resolve the gas kinematics, and (3) KCWI has a relatively large field-of-view (FoV) to cover extended Ly $\alpha$  nebulae. Furthermore, KCWI nicely complements the characteristics of MUSE which thrives at  $\lambda > 5000\text{\AA}$ .

Data was taken with the Keck/KCWI instrument between November 15 2017 and January 30 2019. The seeing varied in the range of 0.7 – 1.1 arcsec (FWHM of the Gaussian at  $\approx 4000\text{\AA}$ , measured in the combined 40 min datacubes). The information of the QSO fields are summarized in Table 1.

For our program, we configured KCWI with the BM grating and medium slicer which yields a FoV of  $16.8''$  perpendicular to slicer (24 slicers) and  $20''$  along the slicer. We also use BM grating and large slicer to observe one of our QSOs: Q1444

This FoV is sufficient to map the gas around QSO host halos to a radius of  $\approx 100$  kpc at  $z \approx 2.3$ . This setting can provide a spatial sampling of  $\frac{20''}{24 \text{ slicers}} \approx 0.67''$  along the slicer and is seeing-limited perpendicular to the slicer. The spectral resolution is  $R = 4000$ . We observed at central wavelengths ranging from  $\lambda = 3900\text{\AA} - 4100\text{\AA}$  to cover the Ly $\alpha$  emission of each QSO in the sample.

The total exposure time for each target is 40 minutes, which consists of four 10-minute individual exposures. The observing procedure is as follows: we divide the entire QSO sample into several sub-groups, with each sub-group consisting of two to several QSOs separated by  $\lesssim 3$  degrees on the sky. Also, we require that the redshift offset  $\Delta z$  between each of our QSOs is greater than  $|\Delta z| > 0.05$ . This procedure was taken because the sky is determined using a nearby offset-target with Ly $\alpha$  emission lines at different wavelengths (see details in §2.3.3).

### 2.2. KCWI QSO Sample at $z \approx 2$

Our ultraluminous QSO sample at  $z \approx 2$  is selected from the SDSS-IV/eBOSS database (e.g., Pâris et al. 2017), restricted to  $2.1 < z < 2.3$ . The lower limit of  $z = 2.1$  is set by the blue limit to the sensitivity of KCWI. The purpose for constraining  $z \leq 2.3$  is that there is currently no systematic IFU survey at  $z \leq 2.3$ . Further, at this redshift, H $\alpha$  emission can be observed from the ground for additional insight into the mechanism(s) powering Ly $\alpha$  (e.g. Leibler et al. 2018). Our KCWI sample can be compared with previous VLT/MUSE observations at  $z > 3$  (Borisova et al. 2016; Arrigoni Battaia et al. 2019) and Gemini and Keck narrowband surveys at  $z \approx 2.3$  (e.g., Arrigoni Battaia et al. 2016).

We select our QSO sample using the following criteria: (1) ultraluminous QSOs with  $i_{\text{mag}} < 18.5$ ; (2) each source must have at least one other ultraluminous QSOs within 3 degree separation, and with a redshift offset  $|\Delta z| > 0.05$  (see §2.3.3 for details of sky subtraction).

Using these selection criteria, we select 16 QSOs (listed in Table 1). Note that the SDSS QSO density peak is at  $z \approx 2.3$  (e.g., Pâris et al. 2017), providing us a large database for selecting targets. The QSOs selected have a median  $i$ -band magnitude of 17.7, 0.2 magnitude brighter than the median  $i$ -band magnitude of 17  $z \approx 3.1$  QSOs in Borisova et al. (2016), and 0.5 magnitude brighter than the 61  $z \approx 3.2$  QSOs described in Arrigoni Battaia et al. (2019). We further calculated  $L_{1450}$  which is the luminosity  $\nu L_\nu$  at  $\lambda = 1450\text{\AA}$ . For our KCWI QSO sample, the median  $L_{1450}$  is  $1.7 \times 10^{13} L_\odot$ . The luminosity of our  $z = 2$  QSOs, on average, is similar to Arrigoni Battaia et al. (2019). The QSOs of Borisova et al. (2016) have a median luminosity of  $3.2 \times 10^{13} L_\odot$ , i.e.  $1.9 \times$  the median  $L_{1450}$  of our KCWI QSO sample. We summarize the QSO luminosity of the three samples in Figure 1.

### 2.3. Data Reduction

In this section, we provide a detailed description of the data reduction, including the standard KCWI pipeline and our post-processing steps using the CubeExtractor package (Cantalupo et al. 2019).

#### 2.3.1. KCWI Standard Pipeline

The KCWI pipeline v1.0\*, released in Mar. 17, 2018 was adopted to reduce our data (Morrissey et al. 2018; Cai et al. 2018). For each image, we first subtracted the bias, correcting the pixel-to-pixel variation using flat-field images, removing cosmic-rays, and error image creation. Then, continuum-bar images were used to conduct a geometric transformation, and the ThAr arc images were analyzed for wavelength calibration. At this stage, the datacube was constructed. Then, the twilight flats were used to correct the slice-to-slice variance. Each individual image was flux calibrated using a spectrophotometric standard star taken at the beginning of the night.

#### 2.3.2. CubeFix: Improving the Flat-fielding of the Cubes

Our scientific goals require the analysis of diffuse, extended emission at low surface brightness. Therefore, we must control for systematic variations across the datacube. We used custom tools for flat-fielding correction and sky-subtraction. The procedures are part of the CubeExtractor package (Cantalupo et al. 2019) which was developed to improve the detection of faint, low surface brightness emission in IFU datacubes (e.g. MUSE, Borisova et al. 2016). We used the CubeFix routine to correct the systematic errors due to flat-fielding. Then, we constructed a medium-band image which is collapsed using 300 channels in the wavelength direction. The slice-by-slice correction is then calculated using the medium-band image. The flat-fielding correction is performed as a self-calibration using sky-lines and sky continuum as a uniform source to re-calibrate each individual slice of the IFU. Sources are masked in this procedure to minimize the self-calibration errors. With these steps, the residual is at a level of less than 0.1% of the sky.

#### 2.3.3. Sky Subtraction and Coaddition

Sky-subtraction was then performed on each individual, flat-field corrected cube using our custom procedure

(CubeSharp routine in the CubeExtractor package). As noted above, we have associated each QSO with another that lies within three degree separation on the sky. We estimate the sky, channel-by-channel, from the unsubtracted datacube of the offset-target. The sky is calculated by taking the median after masking sources. In each wavelength, all pixels with  $3\text{-}\sigma$  above the median were masked as sources, and we repeated this process 10 times to construct a final source mask. The offset-target always has a redshift offset of  $\Delta z > 0.05$  from the main target ( $\Delta z > 0.05$  corresponds to  $\gtrsim 120$  wavelength channels). This criterion insures that the Ly $\alpha$  emission of the offset-target lies far from the emission from the target so that we can use the sky determined from the offset-target field around the wavelength of target's Ly $\alpha$  emission. For each exposure, we determined the QSO center; and then aligned each exposures according to this value. We performed a weighted mean with inverse variance weighting to construct the final datacube. The variance images we used are generated from the KCWI pipeline. The seeing condition for each target has been taken into account in each variance images. The variance amplitude is proportional to the inverse of the seeing full-width-half-maximum (FWHM).

#### 2.4. Point-spread-function (PSF) and Continuum subtraction

To search for extended, faint Ly $\alpha$  emission distinct from the QSO flux, we applied the following procedure to subtract the central, QSO emission. For each wavelength channel, we produce a pseudo-narrowband image with a width of 300 spectral channels ( $\approx 150\text{\AA}$ ). For our analysis, we used the median of these  $\approx 300$  wavelength channels for constructing the pseudo-broadband images. We found that the number of wavelength channels we adopted provides a good compromise between capturing wavelength PSF variations and obtaining a good signal-to-noise ratio in the pseudo-broadband image. Then, we rescaled the empirical PSF according to the integrated flux within the  $1'' \times 1''$  area around the QSO centroid. Then, we subtracted the PSF at each wavelength channel (e.g., Herenz et al. 2015; Borisova et al. 2016). We computed the rescaling factor using an averaged-sigma-clip algorithm to minimize cosmic ray effects.

We further removed continuum sources in each spaxel (a spectrum in the datacube) of the cube using a median-filtering approach to construct a continuum image. The window size of the median filter is approximately 300 pixels ( $\approx 150\text{\AA}$ ). We then subtract the continuum image from each wavelength channel to construct a continuum-subtracted datacube. Sources with flat continua are expected to be eliminated with this procedure. In several cases, stars or background galaxies are not completely removed or are over-subtracted by this procedure due to the large window size. However, these residuals do not affect our results because we mask stars or galaxies with bright continuum in the cube before extraction.

In the left panel of Figure 2, we show the data product just after processing by the KCWI standard pipeline. In the right panel of Figure 2, we provide the individual data after applying all of the post-process reduction described in this section. For low surface brightness measurements, the sky subtraction is crucial. In the final

\* <https://github.com/kcwidev/kderp/>

datacube, we checked that of the sky subtraction residual at wavelengths outside Ly $\alpha$  emission. In our final datacube, the typical 1- $\sigma$  uncertainty is  $\approx 9.0 \times 10^{-19}$  erg s $^{-1}$  cm $^{-1}$  arcsec $^{-2}$  (1 $\text{\AA}$  wavelength bin). The root-mean-square (rms) around zero within an aperture of 2'' is  $\pm 4.5 \times 10^{-19}$  erg s $^{-1}$  cm $^{-1}$  arcsec $^{-2}$  in the rest-frame wavelength channels between 1255 $\text{\AA}$  – 1275  $\text{\AA}$ , a wavelength range that does not contain obvious emission lines from QSOs. These results indicate that our sky subtraction and PSF subtraction are effective.

### 3. RESULTS

After performing the set of careful reduction steps described in the last section, the 1- $\sigma$  flux density uncertainty per voxel<sup>†</sup> is about 1- $\sigma$  of  $\approx 3.5 \times 10^{-19}$  erg s $^{-1}$  cm $^{-2}$   $\text{\AA}^{-1}$  around the observed wavelength of 4000 $\text{\AA}$ . This measurement is consistent with the 1- $\sigma$  error in surface brightness we reported in the previous section. In §2.4, we further checked our sky-subtraction and PSF subtraction, and we confirm that the flux density in the sky-subtracted, PSF-subtracted cubes is consistent with zero within the rest-frame wavelengths  $\lambda = 1255 - 1275$   $\text{\AA}$ . In this section, we carefully analyze the physical properties of Ly $\alpha$  nebulae around the QSO sample at  $z \approx 2$ .

#### 3.1. Optimal Extraction of the Ly $\alpha$ Nebulae

We use the three-dimensional, automatic algorithm CubExtractor (Cantalupo et al. 2019) to conduct optimal extraction of extended Ly $\alpha$  emission in each datacube. We first smooth the datacubes and variance using a Gaussian filter with  $\approx 1'' \times 1''$  aperture. Then, objects are extracted and detected if they contain at least six connected voxels above a signal-to-noise (S/N) of two after smoothing both the signal and the variance<sup>‡</sup>. The three-dimensional segmentation masks output by CubExtractor are then used for our analysis.

In Figure 3, we present the optimally extracted images of the detected objects in each KCWI datacube as done by Borisova et al. (2016). Each image has an angular size of 16.8''  $\times$  20'' FoV. The images have been generated by (i) selecting all voxels in the PSF-subtracted and continuum-subtracted KCWI cubes, (ii) applying the corresponding 3-D masks of each nebula output by CubExtractor, and then (iii) integrating the flux along the wavelength direction. These images are similar to pseudo-NB images, but the width of the filter is adjusted for each spaxel to include only signal above S/N > 2. The width of the pseudo-filter varies from one channel (typically at the edges of the object) to a few tens of wavelength channels in the brightest parts of the sources. The white contour in Figure 3 represents the 2- $\sigma$  uncertainty of SB  $\approx 1.8 \times 10^{-18}$  erg s $^{-1}$  cm $^{-2}$  arcsec $^{-2}$ . The SB uncertainty is calculated in 1 arcsec $^2$  area and in a wavelength bin of 1 $\text{\AA}$  (also see Arrigoni Battaia et al. (2019)).

<sup>†</sup> voxel: a three-dimensional datapoint in an integral field spectrograph datacube.

<sup>‡</sup> The reasons of choosing six voxel limit set is the following: To compare with previous work (e.g., Borisova et al. 2016; Arrigoni Battaia et al. 2019), we choose the number of connected voxel close to the seeing value. The number of pixels that close to the seeing ( $\approx 1''$ ) is 2 voxels perpendicular to slicer direction (1.3''), and 3 voxels along the slicer direction (0.9''). Thus, we use 6 voxel limit set in the manuscript. Actually, we checked to use  $2 \times 2$  voxel smoothing and  $3 \times 4$  voxel smoothing, and we found that the difference of the surface brightness is less than 1%.

Note the 2- $\sigma$  SB limit is slightly different field-by-field. We summarize the SB limit for each source in Table 1.

#### 3.2. Detection rate of giant Ly $\alpha$ nebulae

Above our KCWI detection limit of  $\approx 1.8 \times 10^{-18}$  erg s $^{-1}$  cm $^{-1}$  arcsec $^{-2}$ , we find that 14 out of 16 QSOs in our sample have a detected nebula with diameter  $\gtrsim 50$  kpc. Among them, Q1227, Q1228, Q1230, and Q1416 are enormous Ly $\alpha$  nebulae at  $z \approx 2$  with the SB<sub>Ly $\alpha$</sub>  >  $10^{-17}$  erg s $^{-1}$  cm $^{-2}$  arcsec $^{-2}$  for  $\geq 100$  kpc, and their projected sizes exceed the FoV of KCWI. Q0048 and Q1426 fields contain compact Ly $\alpha$  emitters in the KCWI fields, possibly indicating a strong overdense nature in these fields.

#### 3.3. Surface brightness of the Ly $\alpha$ Emission

In this section, we measure and present the radial Ly $\alpha$  profiles of the nebulae. For comparison with previous works, we use circular-averaged surface brightness (SB) profiles centered on the QSO continua. The SB profile is calculated using the pseudo-narrowband images. We integrate over a fixed velocity range of  $\pm 1000$  km s $^{-1}$  around the centroid of Ly $\alpha$  nebular emission to calculate the surface brightness. This allows us to properly compare the SB calculated in our sample with previous work (e.g., Borisova et al. 2016; Arrigoni Battaia et al. 2019).

The individual, circularly-averaged SB profiles for each QSOs are shown as light gray lines in Figure 4 and Figure 5. Further, we calculated the median SB using the full KCWI QSO sample at  $z \approx 2.2$  (shown in the thick red color in the Figure 4 and Figure 5). In Figure 6, we show the annulus (white circles) which are used to calculate the surface brightness in Figure 4 and Figure 5 for each QSO. We marked the centers of each QSO position using the filled black circle. We found that the median Ly $\alpha$  SB can be described by the following power-law profile centered at the QSO and valid on the radius of  $r \approx 15 - 70$  kpc:

$$SB_{\text{KCWI}}(z \approx 2.3) = 3.7 \times 10^{-17} \times (r/40 \text{ kpc})^{-1.8} \text{ erg s}^{-1} \text{ cm}^{-2} \text{ arcsec}^{-2} \quad (1)$$

Borisova et al. (2016) have conducted a MUSE snapshot survey on 17 QSOs at  $z \geq 3.1$ , and found that all of them are associated with large Ly $\alpha$  nebula on a spatial extent of  $\geq 100$  kpc. Here, we denote the SB of Borisova et al. (2016) as SB<sub>B</sub>. The median SB<sub>B</sub>(Ly $\alpha$ ) can be described by the following equation:

$$SB_{\text{B}}(z \approx 3.1) = 3.2 \times 10^{-17} \times (r/40 \text{ kpc})^{-1.8} \text{ erg s}^{-1} \text{ cm}^{-2} \text{ arcsec}^{-2} \quad (2)$$

Using a larger sample of 61 QSOs at  $z \gtrsim 3.2$ , Arrigoni Battaia et al. (2019) also found that the stacked QSO profiles can be fitted with an exponential profile with  $SB(r) = C_e \exp(-r/r_h)$  or a power law  $SB(r) = C_p r^\alpha$ . These QSOs are characterized by a median redshift of  $z = 3.17$  ( $3.03 < z < 3.46$ ), absolute  $i$  magnitude in the range  $-29.67 \leq M_i \leq -27.03$  similar as that of Borisova et al. (2016). Here, we denote SB<sub>A</sub> as the median surface brightness derived from Arrigoni Battaia et al. (2019) sample. Arrigoni Battaia et al. (2019) found that the obtained stacked profiles may be better fit by

an exponential profile with scale length of  $r_h = 15.2 \pm 0.5$  kpc for radio-quiet objects, i.e.,

$$SB_A(z \approx 3.1) = 5.4 \times 10^{-17} \exp(-r/15.2 \text{ kpc}) \quad (3)$$

$$\text{erg s}^{-1} \text{ cm}^{-2} \text{ arcsec}^{-2}$$

Here, if we correct for cosmological SB dimming of MUSE (Borisova et al. 2016; Arrigoni Battaia et al. 2019) from  $z \approx 3.1$  to  $z = 2.2$ , then the redshift-scaled median SB of the MUSE observations are:

$$SB_B^{\text{scaled}}(z \approx 2.3) \approx 7.6 \times 10^{-17} \times (r/40 \text{ kpc})^{-1.8} \quad (4)$$

$$\text{erg s}^{-1} \text{ cm}^{-2} \text{ arcsec}^{-2}$$

$$SB_A^{\text{scaled}}(z \approx 2.3) \approx 13.7 \times 10^{-17} \exp(-r/15.2 \text{ kpc}) \quad (5)$$

$$\text{erg s}^{-1} \text{ cm}^{-2} \text{ arcsec}^{-2}$$

where the  $SB^{\text{scaled}}$  means that we corrected the surface brightness profile of both Borisova et al. (2016) ( $SB_B$ ) and Arrigoni Battaia et al. (2019) ( $SB_A$ ) from  $z \approx 3.1$  to  $z \approx 2.3$ , scaled by the cosmological surface brightness dimming of the  $(1+z)^4$  factor. We present the scaled data as the purple and orange points in Figure 4 and Figure 5. Note the error bar is not just the statistical error, and the error bar indicates the 25% – 75% percentile in the Figure 4; and 10% – 90% percentile in the Figure 5 around the median surface brightness of  $z \approx 3$  QSO samples. The median SB of Arrigoni Battaia et al. (2019) is consistent with Borisova et al. (2016). Note the median re-scaled SB of Arrigoni Battaia et al. (2019) is a factor of  $1.5 \times$  that of Borisova et al. (2016) over 20 – 40 kpc in radius, and one can also see this using Eqs.(4) and (5). Both MUSE samples suggest that the re-scaled median SB profiles at  $z \approx 3$  is a factor of 2 –  $3 \times$  our KCWI results at  $z \approx 2$ .

In Figure 4 and Figure 5, we also include Arrigoni Battaia et al. (2016) results, shown as the dashed orange curve with error bars. Using narrowband observations on QSOs at  $z \approx 2$ , Arrigoni Battaia et al. (2016) obtained the median Ly $\alpha$  SB at  $z = 2.2$ , similar to the redshift of KCWI QSO sample. The QSOs used in Arrigoni Battaia et al. (2016) are 1.15 magnitude fainter in  $i$ -magnitude than our KCWI QSO sample. Interestingly, the narrowband Ly $\alpha$  SB is one order of magnitude lower than the KCWI observations. Note the narrow-band sample Arrigoni Battaia et al. (2016) indeed detected extended Ly $\alpha$  in 47% of the fields with maximum projected sizes of  $\lesssim 50$  kpc above  $10^{-17} \text{ erg s}^{-1} \text{ arcsec}^{-2}$ . These fields are consistent with seven QSOs in our KCWI sample. Nevertheless, our KCWI survey detected a larger fraction of bright nebulae compared to the narrowband probes, yielding a much higher median SB profile. In §4, we will discuss several possible reasons for this discrepancy. In Figure 4 and Figure 5, we also plot the Ly $\alpha$  profile of Lyman break galaxies (LBGs) at  $z \approx 3$  (e.g., Steidel et al. 2011) and Ly $\alpha$  emitters (LAEs) (e.g., Wisotzki et al. 2016). From the comparison, the Ly $\alpha$  profile powered by galaxies are much fainter than that powered by QSOs.

In Figure 7, we show the two-dimensional (2D) and the corresponding one-dimensional spectra using a pseudo-slit for each QSO. The pseudo-slit for each nebula is the white contour shown in Figure 3. Each corresponding

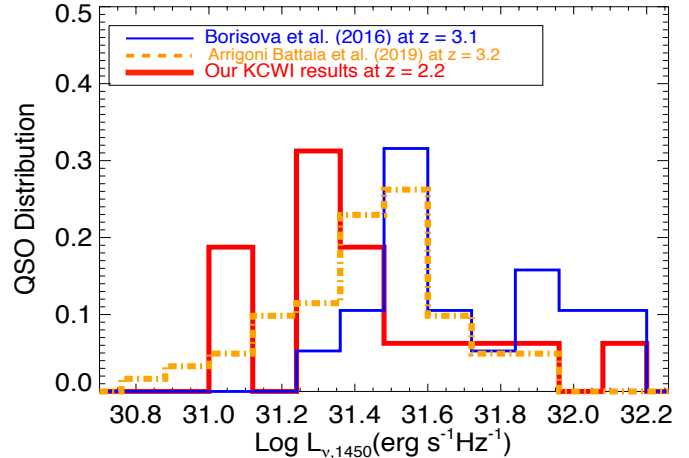


FIG. 1.— The distribution of the QSO luminosity at the rest-frame of 1450 Å at  $z \approx 2$  (Red line). The  $z \approx 2$  QSO sample has a luminosity of  $L_{\nu,1450\text{\AA}} = 10^{31.48 \pm 0.32} \text{ erg s}^{-1} \text{ Hz}^{-1}$ . The blue line represent the QSOs at  $z \approx 3$  from Borisova et al. (2016) which have a QSO luminosity of  $L_{\nu,1450\text{\AA}} = 10^{31.77 \pm 0.25} \text{ erg s}^{-1} \text{ Hz}^{-1}$ . The yellow dot-dashed line represents the QSO luminosity at 1450 Å at  $z \approx 3$  in Arrigoni Battaia et al. (2019) which has a QSO luminosity of  $L_{\nu,1450\text{\AA}} = 10^{31.49 \pm 0.23} \text{ erg s}^{-1} \text{ Hz}^{-1}$ . Our KCWI QSO sample has a similar median bolometric luminosity as Arrigoni Battaia et al. (2019) and is 0.29 dex fainter than Borisova et al. (2016).

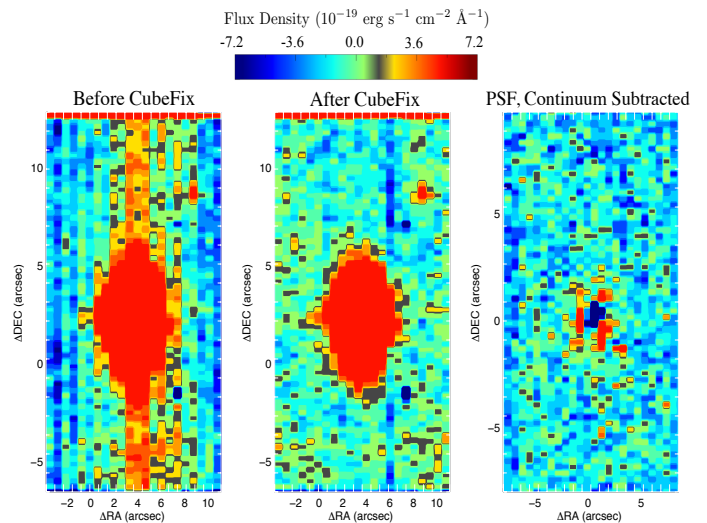


FIG. 2.— Left panel shows a white-light image obtained from a cube reduced with the KCWI standard pipeline (v1.0). Middle cube indicates the data product after running our post-process script CubeExtractor (CubeFix routine). Note that the scattered light is reduced. Right cube shows the Point-spread-function (PSF) and continuum-subtracted cube. The images shown here are constructed using the median of 2000  $\text{km s}^{-1}$  velocity channels between the Ly $\alpha$  and NV region, where we expect no significant line emission in this velocity range, and the median flux is consistent with zero.

1D spectrum is obtained by integrating all spatial pixels within the white contour in Figure 3. In each sub-figure, we detect high S/N Ly $\alpha$  emission line. The extended Ly $\alpha$  emission for each QSO have FWHM of 400 – 800  $\text{km s}^{-1}$ , i.e. much narrower than the QSO Ly $\alpha$  emission (blue spectra in Figure 7). This confirms that the ex-

tended nebular emission is unrelated to PSF subtraction residuals.

### 3.4. Morphology of the nebulae

From Figure 3, each nebula has a different morphology and size. All of them have asymmetric morphology. We use the method of Arrigoni Battaia et al. (2019) to quantify the morphology. Our results can be used to quantify the morphological evolution of the Ly $\alpha$  nebulae from  $z = 3$  to  $z = 2$ . We used the asymmetry of  $\alpha$  to quantify the morphology, and  $\alpha$  can be calculated from the following formulae:

$$\begin{aligned} M_{xx} &\equiv \left\langle \frac{(x - x_{\text{Neb}})^2}{r^2} \right\rangle_f; & M_{yy} &\equiv \left\langle \frac{(y - y_{\text{Neb}})^2}{r^2} \right\rangle_f; \\ M_{xy} &\equiv \left\langle \frac{(x - x_{\text{Neb}})(y - y_{\text{Neb}})}{r^2} \right\rangle_f \end{aligned} \quad (6)$$

where  $x_{\text{Neb}}$ ,  $y_{\text{Neb}}$  are the flux-weighted centroid for each nebulae within the  $2\text{-}\sigma$  isophoto in the 2D image shown in Figure 3, and  $r$  is the distance of a point  $(x, y)$  from the flux-weighted centroid. The subscript  $f$  represents the flux-weighted centroid.

$$Q \equiv M_{xx} - M_{yy}, \quad U \equiv 2M_{xy} \quad (7)$$

where  $M_{xx}$ ,  $M_{xy}$ ,  $M_{yy}$  are called second-order moments (“Stokes parameters”) (see Arrigoni Battaia et al. 2019). Using Eq. (6) and Eq. (7), we define the asymmetry  $\alpha$  using the following equation:

$$\alpha = b/a = \frac{(1 - \sqrt{Q^2 + U^2})}{1 + \sqrt{Q^2 + U^2}} \quad (8)$$

We find that at  $z \approx 2$ , the median of the asymmetry of our 16 QSOs is 0.54, with a  $1\sigma$  scatter of 0.18 (see Figure 9). Note the surface brightness for yielding this results are  $2\sigma$  limit of  $\approx 2 \times 10^{-18} \text{ erg s}^{-1} \text{ cm}^{-2} \text{ arcsec}^{-2}$ . The asymmetry of the nebular morphology does not have a strong dependence of the size of the nebulae. The bright nebulae with diameters  $> 100 \text{ kpc}$  (e.g., Q2123, Q1230, Q1416) show clumpy and filamentary structures. Q2121 shows two major components. Q0048 shows a strongly asymmetric Ly $\alpha$  distribution and a compact Ly $\alpha$  emitter in the field. For a comparison, Borisova et al. (2016) suggest that most nebulae at  $z > 3$  with modest Ly $\alpha$  emission have more symmetric and circular emission; nebulae with scales  $> 200 \text{ kpc}$  show evidence of filamentary structure and complex multiple components. Arrigoni Battaia et al. (2019) also found that most of the nebulae at  $z > 3$  have symmetric and round morphologies, with a median asymmetry of  $\alpha = 0.71$ . One of the most asymmetric structure in the sample is the ELAN in Arrigoni Battaia et al. (2019) with  $\alpha \approx 0.5$ . The  $z \approx 2$  QSOs have a smaller median asymmetry. Although larger sample is required,  $z \approx 2$  QSOs may be more asymmetric and clumpy compared to the  $z \approx 3$  samples (Arrigoni Battaia et al. 2019). We will discuss the implications of these observations in §4.5.

### 3.5. Kinematics of the Ly $\alpha$ Nebula

Although the Ly $\alpha$  line may be broadened by radiative transfer effects, the relative comparison between the kinematics of different objects is still informative. In Figure 10, we show the map of the first moment (flux-weighted velocity) for each Ly $\alpha$  nebula, centered on the peak of the integrated Ly $\alpha$  emission of each nebula. Q1416, Q1228, may show possible rotation kinematics in disk-like structures, possibly suggesting kinematics of gas inflow predicted by simulations (e.g., Stewart et al. 2013). Nevertheless, the majority of the nebulae do not show any clear evidences of rotation or well-regulated kinematic patterns.

In Figure 11, we present the velocity dispersion map (the second moment of the flux distribution). The median value of the velocity dispersion for each sources ranges from  $83 - 381 \text{ km s}^{-1}$  §. Our current data does not suggest any clear correlation between the luminosity and the velocity dispersion of Ly $\alpha$  emission (Figure 12). The velocity dispersion shown in Figure 11 is consistent with the FWHM calculated from the integrated spectra shown in the Figure 7. The velocity dispersion of  $z \approx 2$  QSOs have a consistent range with that of  $z \approx 3$  (Borisova et al. 2016; Arrigoni Battaia et al. 2019). The motions within Ly $\alpha$  nebularities have amplitudes consistent with gravitational motions expected in dark matter halos hosting QSOs ( $M_{\text{halo}} \sim 10^{12.5} M_{\odot}$ ) at these redshifts (e.g., Arrigoni Battaia et al. 2019).

## 4. DISCUSSIONS

From the analysis presented in the §3, it is clear that our KCWI observations reveal extended Ly $\alpha$  emission on the projected scales exceeding  $50 \text{ kpc}$  around 14 out of 16 of the  $z \approx 2$  QSOs (except Q0848 and Q2125). Further, the median surface brightness of Ly $\alpha$  in the KCWI study is higher than that of previous narrowband studies at similar redshift. KCWI results suggest that the typical circularly-averaged SB profile of Ly $\alpha$  nebulae at  $z \approx 2$  is a factor of  $2 - 3$  lower than that at  $z \approx 3$  determined by MUSE observations (e.g., Borisova et al. 2016; Arrigoni Battaia et al. 2019). In this section, we discuss the implications of the observations, relying only on the information coming from the KCWI observations.

### 4.1. A much higher detection rate of Ly $\alpha$ nebulae at $z \approx 2$ compared to narrowband surveys

The results of the KCWI survey at  $z \approx 2$  is in contrast with previous narrowband studies at the same redshift. In our KCWI survey, 14 out of 16 QSOs at  $z \approx 2$  are associated with Ly $\alpha$  nebulae having projected linear scales of  $> 50 \text{ kpc}$ , with the  $2\text{-}\sigma$  SB limit of  $2 \times 10^{-18} \text{ erg s}^{-1} \text{ cm}^{-2} \text{ arcsec}^{-2}$ . The median profile is  $SB_{\text{Ly}\alpha} = 3.7 \times 10^{-17} \times (r/40 \text{ kpc})^{-1.8} \text{ erg s}^{-1} \text{ cm}^{-2} \text{ arcsec}^{-2}$  (see §3).

The KCWI survey reaches a typical  $2\text{-}\sigma$  SB of  $1.6 \times 10^{-18} \text{ erg s}^{-1} \text{ cm}^{-2} \text{ arcsec}^{-2}$  ( $1 \text{ \AA}$  wavelength bin), deeper than previous narrowband surveys (typically  $\approx 4 \times 10^{-18} \text{ erg s}^{-1} \text{ cm}^{-2}$  in Arrigoni Battaia et al. (2016)). The luminous, large Ly $\alpha$  emission detected in our KCWI survey is rarely found in previous narrowband survey. We use dashed yellow error bars in (Figure 4 and Figure 5)

§ Note the FWHM of the emission line if Gaussian is approximately a factor of  $2.35 \times$  the velocity dispersion.

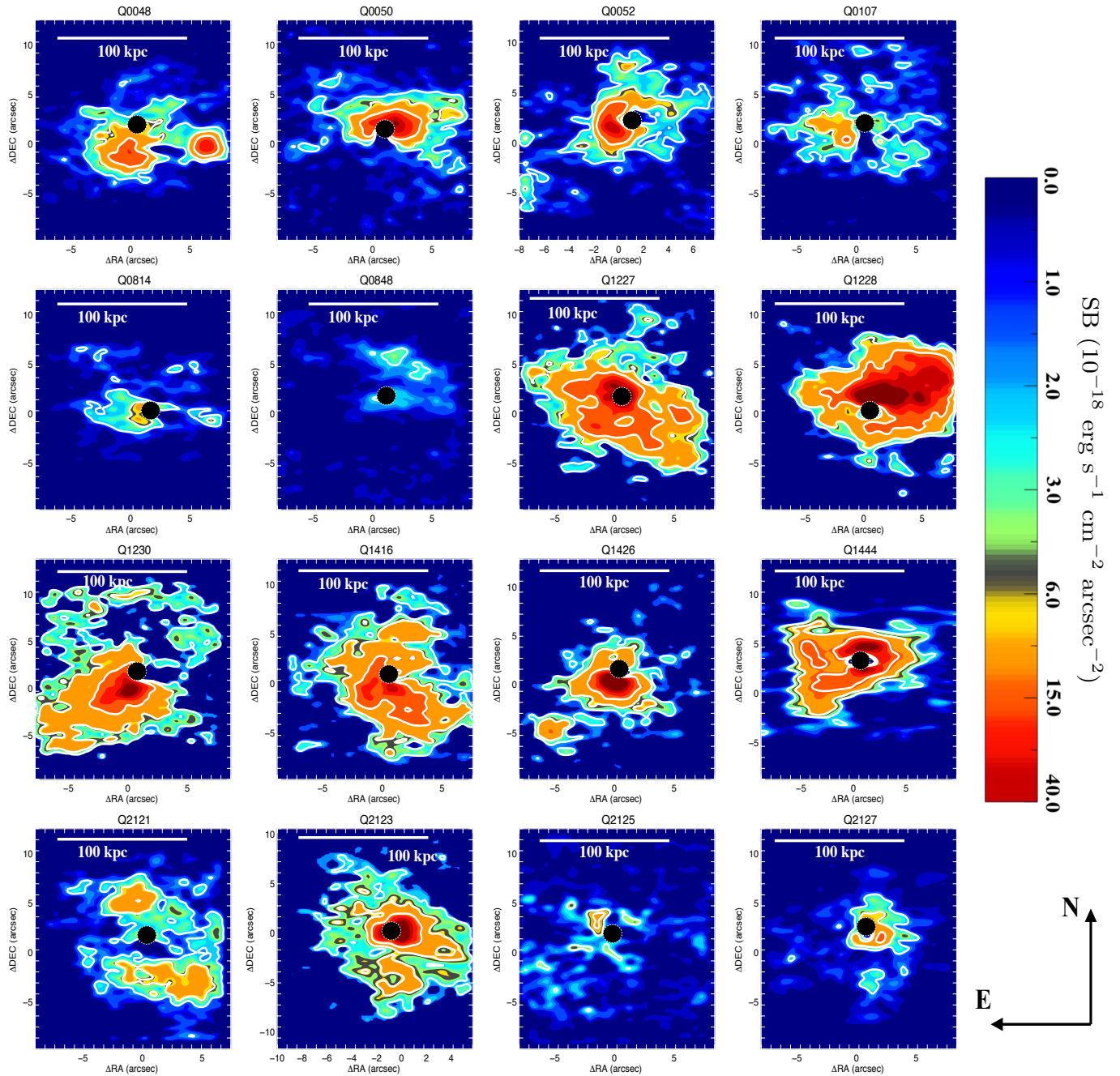


FIG. 3.— “Optically-extracted” Ly $\alpha$  images from PSF and continuum-subtracted KCWI datacubes for each QSO. The white bar indicates a physical scale of 100 kpc. Each image has a size of  $16''$  in x-axis and  $20''$  in y-axis. The images have been produced by collapsing the datacube voxels associated with the CubExtractor 3-D segmentation maps (the “3D-mask”) along the wavelength direction (see §2). The SB is calculated using the CubExtractor 3D segmentation mask that includes a different number of spectral resolution bins. The 3D segmentation masks have been obtained with a signal-to-noise ratio (SNR) threshold of 2 per smoothed voxel, similar to Borisova et al. (2016) and Arrigoni Battaia et al. (2019). The white thick contours in each image corresponds to  $2\text{-}\sigma$ ,  $5\text{-}\sigma$  and  $10\text{-}\sigma$  SB, with  $1\text{-}\sigma_{\text{SB}} = 5 \times 10^{-19} \text{ erg s}^{-1} \text{ cm}^{-2} \text{ arcsec}^{-2}$ . The black dots represent the positions of the central QSOs.

to represent a large narrowband survey (Arrigoni Battaia et al. 2016) which study suggests that the Ly $\alpha$  SB level is  $5 \times 10^{-19}$  erg s $^{-1}$  cm $^{-2}$  arcsec $^{-2}$  at  $R \approx 50$  kpc. The median SB probed by KCWI is about one order of magnitude brighter than that of previous narrowband survey shown in dashed yellow line in Figure 4 and Figure 5.

Let us explore several possibilities that could result in significantly fainter Ly $\alpha$  profiles that were obtained by narrowband surveys at  $z \approx 2$ . We propose the following explanations: (1) light loss due to the narrowband filter; (2) fainter QSOs due to smaller QSO sample constrained by the narrowband.

The first reason could be due to the Ly $\alpha$  line falling outside (or partially outside) the filter. In Figure 7, we marked the systemic redshift of these QSOs using vertical purple lines. Similar to Arrigoni Battaia et al. (2019), for our KCWI sample, we used the systemic redshift determined from SDSS Mg II emission, correcting the luminosity-dependent offset between Mg II and systemic redshift (Richards et al. 2002; Shen et al. 2016). Our QSO sample resides at the bright-end in the SDSS QSO sample, and all of them have a high SNR Mg II emission detected in the SDSS spectra. Note that all QSOs except Q1416, have large systemic redshift offset comparing to that of the nebular Ly $\alpha$  emission. More than 50% of the QSOs have systemic redshifts  $\gtrsim 1000$  km s $^{-1}$  bluer than the Ly $\alpha$  redshift of the extended nebulae. 80% of the QSOs have  $\gtrsim 800$  km s $^{-1}$  velocity offset between nebular Ly $\alpha$  emission and QSO systemic redshift determined by SDSS pipeline ( $z_{\text{pipe}}$  in Table 1). If we use the redshift of principle component analysis (PCA)  $z_{\text{PCA}}$  (e.g., Pâris et al. 2017), we still found that 10 out of 16 have velocity offset  $> 500$  km s $^{-1}$  away from the nebular Ly $\alpha$  redshift. When conducting narrowband surveys, if we require the QSO systemic redshift to be within 500 km s $^{-1}$  from the most sensitive part of the filter, then most of nebular emission would be outside the sensitive part of the filter. For example, the narrowband filter that Arrigoni Battaia et al. (2016) used has a FWHM of 3000 km s $^{-1}$ . Thus, a velocity offset of  $> 1300$  km s $^{-1}$  can significantly reduce the observed Ly $\alpha$  flux and decrease the ability to detect extended emission. In the Figure 8, we present a simulated narrowband image of Q1228. The systemic redshift of Q1228 is 600 km s $^{-1}$  bluer than the Ly $\alpha$  redshift. Using a narrowband with FWHM of  $\approx 30$  Å centered on the systemic redshift (the profile of the filter is the same as the filter used in Arrigoni Battaia et al. 2016), the Ly $\alpha$  emission is very compact. From Figure 8, if the narrowband filter has a central wavelength consistent with the systemic redshift (e.g., Arrigoni Battaia et al. 2016), Ly $\alpha$  is a compact source which is easily missed under the extremely bright PSF in the narrowband imaging. The IFU, compared to narrowband, does not have the narrow redshift constraint, and thus, one can always detect nebular Ly $\alpha$  emission even if the velocity offset between nebular Ly $\alpha$  and QSO systemic is larger than expected.

Due to the wide wavelength coverage afforded by KCWI, the KCWI QSO sample is 1.15-mag brighter than the narrowband QSO sample (Arrigoni Battaia et al. 2016). However, using our sample, we demonstrate that there are no obvious correlation between nebular Ly $\alpha$  and QSO ionizing flux (or QSO magnitude) (see Fig-

ure 13). Thus, there is no strong evidence to support that the 1.15-mag fainter QSO sample to be a major factor for the one order of magnitude discrepancy between the extended nebular Ly $\alpha$  observed by KCWI and narrowband (also see the similar conclusion for  $z \sim 3$  in Arrigoni Battaia et al. (2019)).

#### 4.2. Evolution of the Circularly-Averaged Ly $\alpha$ Surface Brightness from $z \gtrsim 3$ to $z \sim 2$

From Eq. (1) and Eq. (3), Figure 4 and Figure 5, we know that 90% of the  $z \approx 2$  Ly $\alpha$  nebulae have circularly averaged SB profiles fainter than the median SB profiles Ly $\alpha$  SB at  $z \gtrsim 3$  (Borisova et al. 2016; Arrigoni Battaia et al. 2019; also see Marino et al. 2019). The median SB at  $z \approx 2$  is 0.4 dex fainter than the median Ly $\alpha$  SB profile at  $z \approx 3$ . In this section, we investigate possible cause of such an evolution.

Comparing with  $z \approx 3$ , the lower circularly averaged SB at  $z \approx 2$  can be arise from two scenarios: (a) Nebulae at  $z \approx 2$  could have less circular morphology or lower emission cover fraction than that at  $z \approx 3$ . (b) The nebular SB are intrinsically fainter. This could further suggest lower local densities or lower gas mass in the QSO halos at  $z = 2$  compared to  $z = 3$ . Our measurement is based on a sample of 16 QSOs at  $z \approx 2$ , and a larger  $z \approx 2$  QSO sample should be required to further confirm the results in this paper.

##### 4.2.1. Comparison between the Covering Fraction of the Ly $\alpha$ Emitting Cloud at $z \gtrsim 3$ and $z \approx 2$

For scenario (a), we quantify the redshift-corrected area of a characteristic surface brightness. We choose the characteristic surface brightness of  $1 \times 10^{-17}$  erg s $^{-1}$  cm $^{-2}$  arcsec $^{-2}$  which is well detected in each of our KCWI QSOs at  $z \approx 2.3$  and represented in orange color in Figure 3. The fiducial SB at  $z \approx 2.3$  is corresponding to  $\approx 4 \times 10^{-18}$  erg s $^{-1}$  cm $^{-2}$  arcsec $^{-2}$  at  $z \approx 3.1$ . This value is well detected for each QSOs at  $z \approx 3.1$  in MUSEUM QSO survey (Arrigoni Battaia et al. 2019). For all nebulae at  $z \approx 3$ , the SB contours of  $\gtrsim 4 \times 10^{-18}$  erg s $^{-1}$  cm $^{-2}$  arcsec $^{-2}$  at  $z \approx 3.1$  have projected size within the KCWI FoV (Arrigoni Battaia et al. 2019), and thus, the area at  $z \approx 2$  and  $z \approx 3$  can be directly compared without correcting the difference of the FoV between KCWI and MUSE.

In Figure 14, we present the projected area of the nebulae with the SB above the fiducial value, and compared with  $z = 3$  MUSE results (Arrigoni Battaia et al. 2019) with the same scaled SB at  $z = 2$ . From the figure, the median area at  $z = 2$  is about 63 arcsec $^2$  (4340 kpc $^2$ ), this is about 55.1% of the median area of MUSE nebulae of  $A_{\text{median}} = 123$  arcsec $^2$  (7872 kpc $^2$ ). Let us further take into account the halo size from  $z \approx 3 - z \approx 2$ . Let us assume the QSO halo to have a halo mass of  $M_{\text{halo}} \approx 10^{12.5} M_{\odot}$  (e.g., White et al. 2012; Shen et al. 2007) at both redshifts. Under this assumption, the Virial radius of the halo is  $R_{\text{h},z=3.1} \approx 112$  kpc at  $z \approx 3.1$ , and  $R_{\text{h},z=2.3} \approx 138$  kpc at  $z \approx 2.3$ . The covering factor of Ly $\alpha$  emitting region can be estimated using  $4340 \text{ kpc}^2 / (\pi R_{\text{h},z=2.3}^2) \approx 0.07$  at  $z \approx 2.3$ . Using the same method, we estimate that the covering factor of the Ly $\alpha$  emitting at  $z \approx 3.1$  is about 0.19, a factor of 2.7 $\times$  that at  $z \approx 2.3$ . Therefore, we conclude that QSO halos at



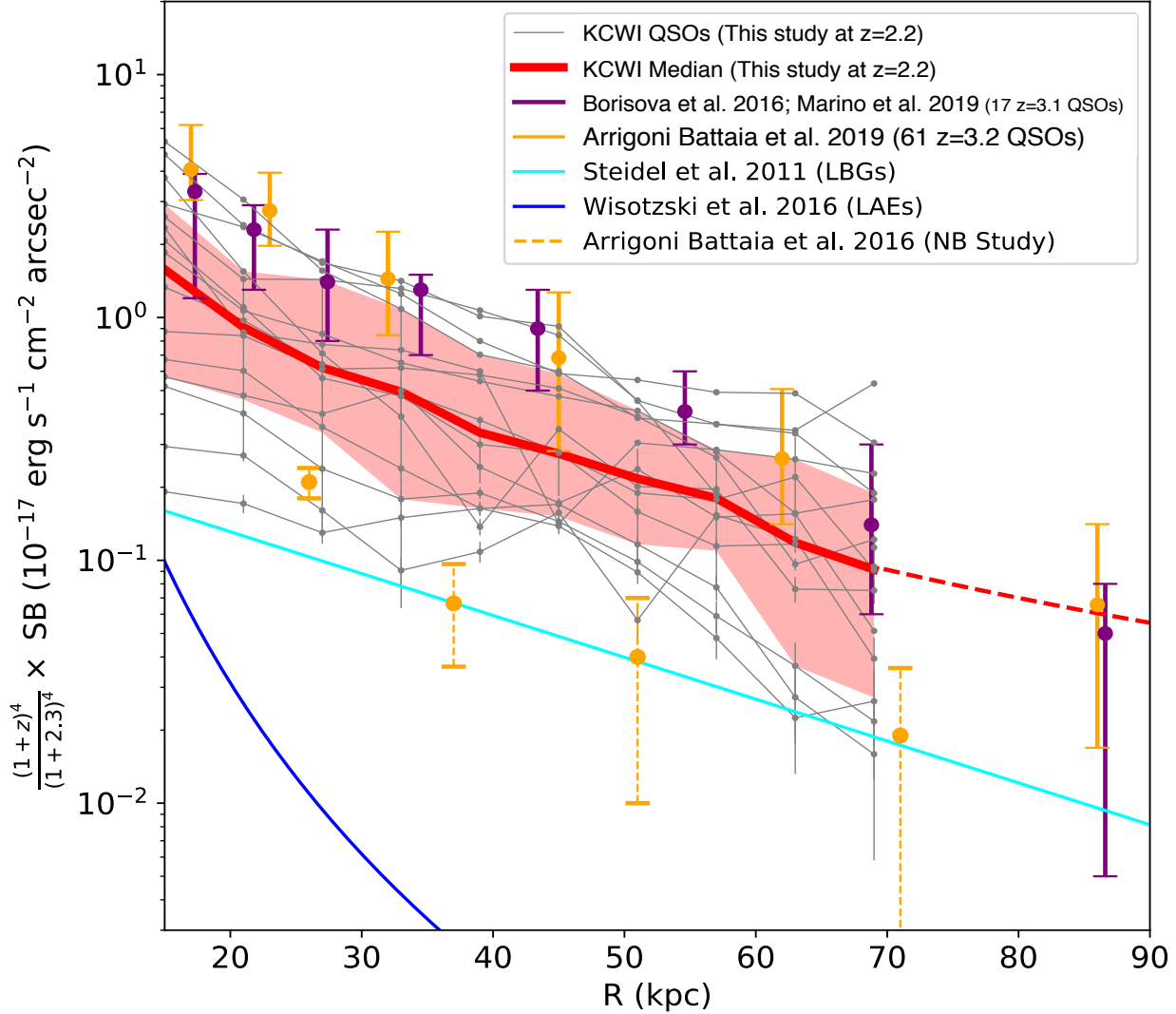


FIG. 4.— Ly $\alpha$  surface brightness (SB) profiles (circularly averaged) as a function of radius around ultraluminous QSOs. All errorbars represent the 25 – 75 percentile of Ly $\alpha$  SB in each QSO sample. The gray line with cyan points represent the SB profile for individual QSO at  $z \approx 2$ . Same as Borisova et al. (2016) and Arrigoni Battaia et al. (2019), the SB is calculated in the pseudo-narrowband images with the width of  $2000 \text{ km s}^{-1}$ , centered on the nebular Ly $\alpha$  emission (§3.3). The thick red curve represents the median Ly $\alpha$  profile of the KCWI sample at  $z \approx 2$ . The solid line is the median of the actual data, and the dashed red curve indicates the extrapolation results. The red region represents the SB within the 25% and 75% percentile of our KCWI QSO sample. Purple represents the median Ly $\alpha$  SB profile of 17 QSOs at  $z \approx 3$  (Borisova et al. 2016) while the error bars represent the 25 and 75 of percentile of this sample. The solid orange with error bar represent the median and 25 – 75 percentile Ly $\alpha$  SB of 61 QSOs at  $z \approx 3.2$  reported by Arrigoni Battaia et al. (2019). Orange points with dashed error bar represent the SB of Ly $\alpha$  emission using a narrowband filter (Arrigoni Battaia et al. 2016). Cyan represents the Ly $\alpha$  SB for Lyman break galaxies (LBGs) at  $z \approx 3$  (Steidel et al. 2011), and blue shows the Ly $\alpha$  profile for  $z \approx 3$  Lyman alpha emitters (LAE) (e.g., Wisotzki et al. 2016).

$z \approx 2$  have a lower covering factor of the Ly $\alpha$  emitting clouds compared to that at  $z \approx 3$ , and the lower covering factor may be one of the main reasons for the evolution of circular-averaged Ly $\alpha$  SB from  $z = 3$  to  $z = 2$ .

We can further use another independent method to confirm that the lower circularly-averaged SB at  $z \approx 2$  seen in Figure 4 and Figure 5 is due to the lower covering factor. We calculated the median SB in a 90-degree-quadrant for each nebula. ¶ Then, we compute the ratio of the 90-degree-quadrant SB to the full annuli SB. A higher value of this ratio indicates a lower covering factor or a more asymmetric distribution of the Ly $\alpha$  emitting regions. In the right panel of Figure 15, we plot the ratio of the SB in a 90-degree-sector \*\* to the median SB in the full annuli. We could see that this ratio at  $z \approx 2.3$  (red) is higher than that at  $z \approx 3$  (purple) on the scale of 15 – 70 kpc, suggesting that the covering factor of the Ly $\alpha$  emitting clouds at  $z \approx 2$  is lower than that at  $z \approx 3$ . In the left panel of Figure 15, we further show the 90-degree-quadrant, redshift-corrected SB at  $z \approx 2.3$ . Compared to the SB calculated using full annuli, the  $z \approx 2$  and  $z \approx 3$  SB are more consistent with each other, indicating that the characteristic, local Ly $\alpha$  SB within the Ly $\alpha$  emitting regions at  $z \approx 2$  is close to that at  $z \approx 3$ . The dimming of the circularly average SB at  $z \approx 2$  is due to a smaller covering factor of Ly $\alpha$  emitting clouds.

#### 4.2.2. Evolution of the Cosmological Gas Density

From the above section, we have shown that at the fixed SB, our KCWI QSO sample at  $z \approx 2$  has less area covered by Ly $\alpha$  emitting regions compared to QSOs at  $z \approx 3$  Borisova et al. (2016); Arrigoni Battaia et al. (2019). In the following, we investigate the scenario (b): whether the  $z \approx 2$  nebulae are intrinsically fainter, i.e., whether  $z \approx 2$  QSOs have lower CGM densities at  $z = 2$  compared to  $z = 3$ .

The local surface brightness of the Ly $\alpha$  emitting regions between  $z \approx 2$  and  $z \approx 3$  is consistent with each other (left panel of Figure 15). In this section, we further demonstrate that cosmic density evolution may not be a major factor of causing the evolution of the circularly-averaged SB from  $z \approx 3$  to  $z \approx 2$ .

Following the expansion of the Universe, the cosmic mean density evolves as  $(1+z)^{-3}$ . Given the standard convention of defining a dark matter halo as  $200 \times$  the mean density, the density in the halo systematically decreases from  $z = 3 - 2$ . In the standard  $\Lambda$ CDM Universe, the cosmic scale factor  $a(z)$  is proportional to  $\frac{1}{(1+z)}$ . At  $z > 2$ , the cosmic density  $\rho(z)$  is proportional to  $\frac{1}{a(z)^3}$ , and the density at  $z = 3.1$  ( $\rho(z = 3.1)$ ) and that at  $z = 2.3$  ( $\rho(z = 2.3)$ ) have the following relation:

$$\rho(z = 3.1) = \frac{(1 + 2.3)^3}{(1 + 3.1)^3} \times \rho(z = 2.3) = 1.92 \times \rho(z = 2.3). \quad (9)$$

The average density of a halo at  $z = 3.1$  is  $1.92 \times$  the halo at  $z = 2.3$ . If QSO halos follow this general halo density evolution, and further, if the cool gas density is proportional to the halo matter density, then the Ly $\alpha$ -emitting

¶ Quadrant: a sector of 90 degree, and the quadrant is chosen with the highest median SB over a large number of rotations.

\*\* Again, for each QSO, the quadrant is chosen with the highest median SB over a large number of rotations.

cool gas density in QSO halo at  $z = 3.1$  is expected to be  $1.92 \times$  that at  $z = 2.3$ . Then, the  $SB_{Ly\alpha}$  could evolve accordingly as the evolution of cool gas density.

The optically thin photo-ionization model is a favored scenario for nebular Ly $\alpha$  emission around AGN (e.g., Heckman et al. 1991a; Cantalupo et al. 2014; Arrigoni Battaia et al. 2015, 2016; Cai et al. 2017; see also discussions in Cai et al. 2018). In the optically thin approximation, the Ly $\alpha$  surface brightness  $SB_{Ly\alpha} \propto n_H N_H$ , where  $n_H$  is the number density of the hydrogen, and  $N_H$  is the column density which is also proportional to the gas number density. From above, we know that the QSO halo density at  $z = 3.1$  could be  $1.92 \times$  the density of halo at  $z = 2.3$ . If the gas in the halo is largely optically thin, then we expect that the  $SB_{Ly\alpha} \propto n^2$ , where  $n$  is the gas density. Then, we expect:

$$SB_{Ly\alpha, z=2.3} = \frac{1}{3.7} \times SB_{Ly\alpha, z=3.1}, \quad (10)$$

The Equ.(8) suggests that if the dimming of the circular-averaged SB is due to the global evolution of the CGM density, then the characteristic redshift-dimming-corrected  $SB_{Ly\alpha}$  at  $z \approx 3.1$  could be a factor of  $3.7 \times$  that at  $z \approx 2.3$ . This is not consistent with our current observations. As described in the previous section, the characteristic Ly $\alpha$  emission at  $z \approx 2$  is consistent with that at  $z \approx 3$ , but  $z \approx 2$  halo has a lower covering factor comparing to  $z \approx 3$ . This suggests that the local densities of the cool, Ly $\alpha$ -emitting gas have little evolution from  $z \approx 3 - z \approx 2$  as the cosmic expansion, as expected from cosmological theories (the CGM is not in the linear part of the growth of perturbations).

Note the above conclusion is drawn under the optically thin photoionization scenario. The optically thick photoionization is not favoured by our observations. If the Ly $\alpha$  nebular emission is mainly contributed by optically thick gas, then the strong correlation between the luminosity of Ly $\alpha$  ( $L_{Ly\alpha}$ ) and the QSO ionizing luminosities should exist. Nevertheless, from Figure 13, there are no obvious correlation between nebular  $L_{Ly\alpha}$  and the QSO ionizing luminosities in our sample<sup>††</sup>, indicating optically thick scenario is not favoured by our observations.

#### 4.2.3. Evolution of Mass Threshold of Hot Halo

The decreasing of the Ly $\alpha$  emitting regions from  $z \approx 3$  to  $z \approx 2$  may also be interpreted using the mechanisms of the cool gas penetration in the massive halos (Dekel et al. 2009). Dekel et al. (2009) study the penetration of cold gas into the halo as a function of halo mass and redshift. They find that, from the simulation, halos at  $z \gtrsim 3$  with  $M > 10^{13} M_\odot$  are dominated by hot gas, but at  $z \approx 2$ , the mass threshold of hot halo decreases

†† The ionizing luminosity of the QSO is determined by rescaling the composite spectrum from Lusso et al. (2015) to the QSO luminosity at the rest-frame 1350 Å. If the gas is optically thick to Lyman continuum photons ( $N_{HI} \gtrsim 10^{17.2} \text{ cm}^{-2}$ ), the cool gas will behave like a mirror and the SB thus follows the relation  $SB_{Ly\alpha} \propto L_{\nu LL}$  (Hennawi & Prochaska 2013). If the source is bright enough to keep the gas highly ionized, i.e., the gas is optically thin ( $N_{HI} < 10^{17.2} \text{ cm}^{-2}$ ). It can be shown that (Hennawi & Prochaska 2013) the Ly $\alpha$  surface brightness is  $SB_{Ly\alpha} \propto n_H N_H$ . Therefore, in the optically thin regime, the observed surface brightness should not depend on the luminosity of the targeted QSOs, but on the density of cool gas.

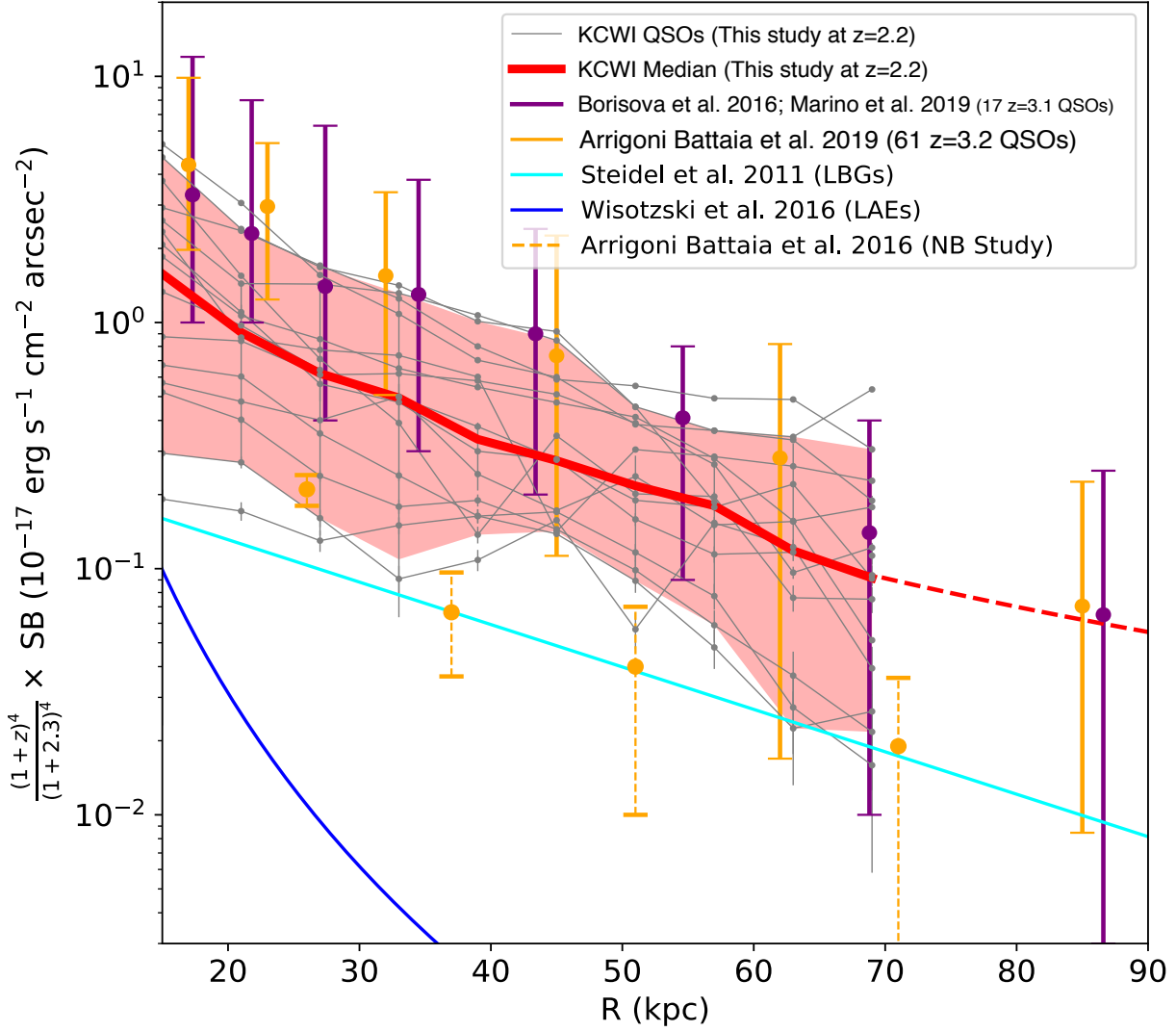


FIG. 5.— Similar to Fig. 4, but showing 10 – 90 percentile of the Ly $\alpha$  surface brightness of each QSO sample.

to  $M \approx 10^{12} M_{\odot}$ . This indicates that QSO halos with a typical halo mass of  $M \sim 10^{12.5} M_{\odot}$  (e.g., White et al. 2012) is more likely to be dominated by hot gas at  $z \approx 2$  while significant amount of cool gas could still penetrate such halos at  $z \approx 3$ . This effect may reduce the surface brightness of Ly $\alpha$  emission from  $z \approx 3$  to  $z \approx 2$ . Note that the cool gas penetration scenario would hold for any Ly $\alpha$  powering mechanisms (see Arrigoni Battaia et al. (2019)), i.e., the decreasing of the cool gas penetration in massive halos may yield a decrease of the Ly $\alpha$  emission. More quantitative analysis on whether this effect can decrease the covering factor of cool gas should be further studied by simulations, combined with deeper observations on other transition lines.

#### 4.3. Ly $\alpha$ morphology and its Evolution from $z \gtrsim 3$ to $z \approx 2$

##### 4.3.1. Summary of the Ly $\alpha$ Morphology at $z \approx 2$ in our KCWI sample

From Borisova et al. (2016) and Arrigoni Battaia et al. (2019), the majority of the MUSE radio-quiet nebulae at  $z \gtrsim 3$  have symmetric morphology. In particular, nebulae with scales smaller than 100 kpc have circular morphologies. Nevertheless, our new KCWI observations suggest that nebulae at  $z \approx 2$  have more irregular and asymmetric morphologies. In the following, we briefly comment on the morphology, kinematics and surface brightness of individual nebula.

From Figure 3, we observe that Q2121 has two spatially distinct components, with a projected separation of  $\approx 85$  kpc. From Figure 7, the two components have similar velocity and the entire Ly $\alpha$  emission has a FWHM of  $\approx 500$  km s $^{-1}$ . Q0048 and Q1426 both have Ly $\alpha$  emitters in the KCWI field of view, at the same redshift with the QSOs, suggesting strongly overdense environment in both fields. The bright Ly $\alpha$  emitter in the Q0048 field is 5'' west of the QSO center. Seven nebulae: Q2121; Q2123; Q1227; Q1228; Q1230; Q1416 have projected scales of  $> 150$  kpc and therefore extend beyond the FoV of the KCWI medium slicer. Their spatial extents are more similar as enormous Ly $\alpha$  nebulae (e.g., Cai et al. 2017; Arrigoni Battaia et al. 2018) with the projected size of  $\gtrsim 200$  kpc. Q2127, Q0814, Q0107, Q2125 and Q0848 are among the lowest Ly $\alpha$  surface brightness in the sample whose projected scales are  $< 100$  kpc. Our KCWI observations suggest that nebulae around QSOs at  $z \approx 2$  may be generally more asymmetric, irregular, and having stronger field-to-field variations than that at  $z \approx 3$ .

##### 4.3.2. Evolution of the Ly $\alpha$ Morphology

The morphology of Ly $\alpha$  nebulae contains information about the cool gas distribution and geometry in the halos. Morphology can also be used to directly compare with cosmological simulations (e.g., Weidinger et al. 2005; Cantalupo et al. 2014). In §3.4, we quantified the asymmetry of the Ly $\alpha$  light distribution following Arrigoni Battaia et al. (2019). From §3.4, we found that the median ratio between the semiminor axis and semimajor axis at  $z \approx 2$  is  $\alpha_{z=2} = 0.54$ , with a scatter of 0.19. For a comparison, at  $z \approx 3$ , Arrigoni Battaia et al. (2019) measured the average ratio of  $\langle \alpha_{z=3} \rangle = 0.71$ , with a scatter of 0.13 (also see Figure 9). This tentatively suggests that nebulae at  $z \approx 2$  may be more asymmetric or

clumpy than that at  $z \approx 3$ . Such an asymmetry could further contribute to the lower average surface brightness at  $z \approx 2$ . This can be further seen from Figure 7 which the 2D spectra of the nebulae at  $z \sim 3$  (Borisova) look smooth in the velocity space, while nebulae in the current survey at  $z \sim 2$  in our sample are more clumpy.

Galaxy structure is a powerful method for determining whether a galaxy is undergoing a recent major merger. Lotz et al. (2008, 2010) find that the asymmetry is sensitive to mergers with mass ratios of 1:4 or less. The halo morphological merger fraction increases from  $z \approx 3 - 2$  and decreases from  $z = 2 - 1$ . The merger fraction is highest around  $z \approx 2$  (e.g., Conselice et al. 2008). Lopez-Sanjuan et al. (2009) further point out that the merger rate at  $z \approx 2$  could be a factor of  $2\times$  that at  $z \gtrsim 3$ . Such an increased merger fraction at  $z \approx 2$  may result in the asymmetric gas morphology we observe at  $z \approx 2$ .

#### 4.4. Offsets between the systemic redshift and Ly $\alpha$ redshift

As indicated in §4.1, we consider three cases: (1) systemic redshift determined from SDSS pipeline ( $z_{\text{pipe}}$ ); (2) systemic redshift determined by Mg II emission ( $z_{\text{MgII}}$ ), correcting the luminosity-dependent small and known offset between Mg II and systemic redshift (Richards et al. 2002; Shen et al. 2016); and (3) systemic redshift determined by the principal component analysis, with the reference sample has been chosen to have an automated redshift corresponding to the location of the maximum of the Mg II emission line ( $z_{\text{PCA}}$ ). These three redshifts are all drawn from the SDSS DR12 QSO catalog (Pâris et al. 2017).

The uncertainties of these redshifts are known to be  $\delta_z \sim 0.003$  ( $\approx 300$  km s $^{-1}$ ) (also see Arrigoni Battaia et al. 2016). In Figure 7, we show the systemic redshift determined by SDSS pipeline ( $z_{\text{pipe}}$ ) (purple vertical line) relative to the center of the integrated nebular Ly $\alpha$  emission (marked as zero in the x-axis). We further show the center of QSO Ly $\alpha$  emission using the orange vertical line. We calculate the velocity shift ( $v_{\text{off}}$ ) between the Mg II-derived systemic redshift ( $z_{\text{sys}}$ ) and the nebular Ly $\alpha$  redshift ( $z_{\text{Neb,Ly}\alpha}$ ), and the expression is as follows:

$$v_{\text{off}} = (z_{\text{sys}} - z_{\text{Neb,Ly}\alpha}) / (1 + z_{\text{Neb,Ly}\alpha}) \times c \quad (11)$$

The velocity shifts range from -3947 to +813 km s $^{-1}$ , with a median velocity shift of -1081 km s $^{-1}$ . In our KCWI sample, only Q1416 and Q2125 have the  $z_{\text{sys}}$  redshifted than the nebular Ly $\alpha$  redshift ( $z_{\text{Ly}\alpha}$ ). All other QSOs (87% of our sample) have  $z_{\text{sys}}$  blueshifted than the nebular Ly $\alpha$  redshift. Similar results have already been reported in Arrigoni Battaia et al. (2019) at  $z \approx 3$ : at  $z \approx 3$ , Arrigoni Battaia et al. (2019) show that the velocity shift between the QSO systemics and the nebular Ly $\alpha$  redshift range  $-6000 \text{ km s}^{-1} \leq v_{\text{offset}} \leq 2000 \text{ km s}^{-1}$ , and 80% nebularities have negative velocity shifts, with the median value of  $\Delta v_{\text{median}} = -782 \text{ km s}^{-1}$ . Similar results and discussions can also be found in Arrigoni Battaia et al. (2019). Note that if we use  $z_{\text{PCA}}$  as the systemic redshift, then the velocity offset ranges from  $-4281 \text{ km s}^{-1} - 1463 \text{ km s}^{-1}$ , with the median velocity offset of  $-553 \text{ km s}^{-1}$ , with the 1- $\sigma$  scattering of 1417 km s $^{-1}$ . If we use  $z_{\text{MgII}}$  as the systemic redshift, the velocity shifts range from  $-1586 \text{ km s}^{-1}$  to  $1646 \text{ km s}^{-1}$ , with the

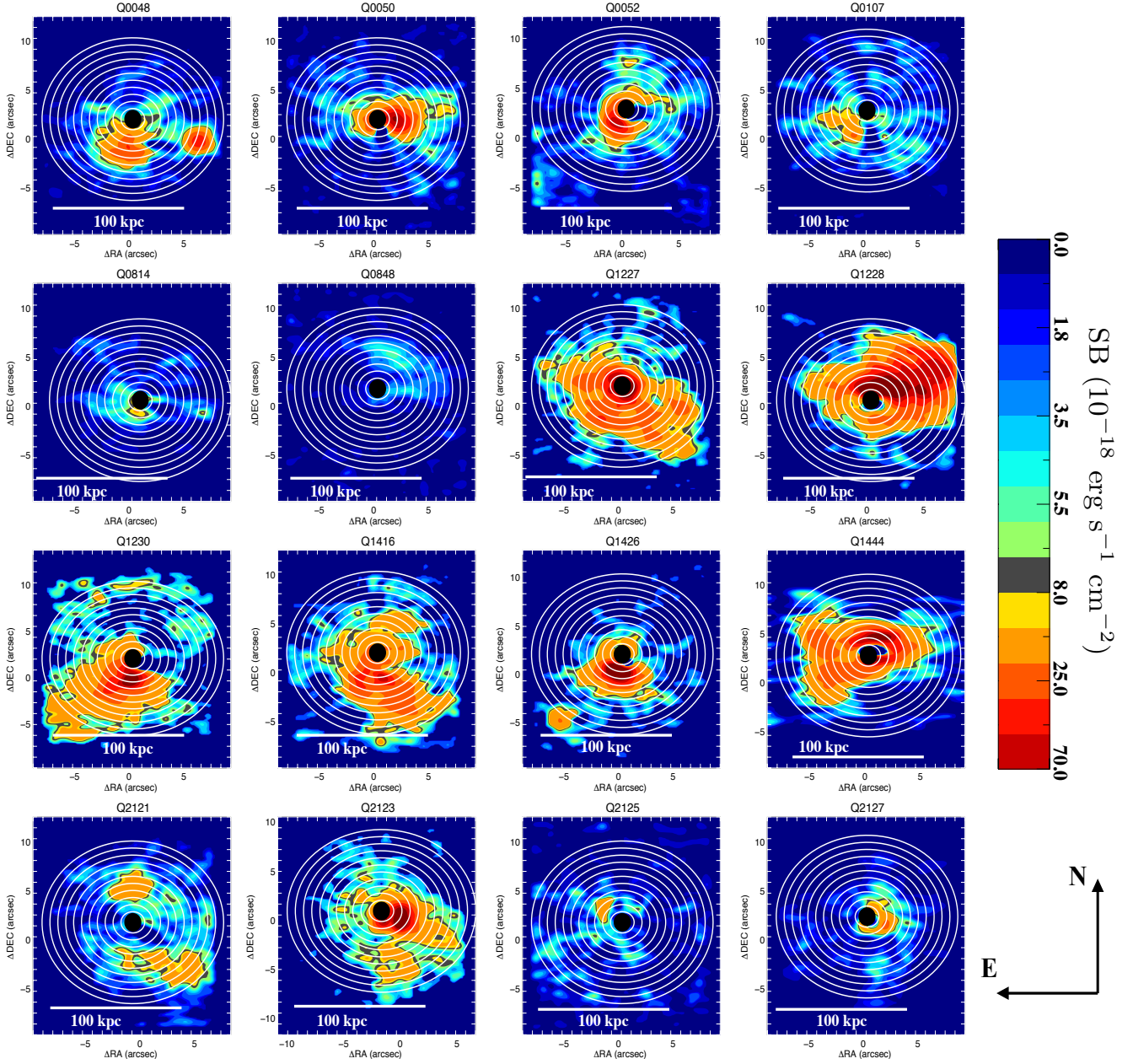


FIG. 6.— In this figure, we present the annuli (white circles) which are used to calculate the surface brightness in Figure 4 and Figure 5 for each QSO. Also, the black filled circle in the center represents the QSO position which is used to calculate the circularly averaged SB profiles.

median offset of  $-92 \text{ km s}^{-1}$ , with the  $1\text{-}\sigma$  scattering of  $877 \text{ km s}^{-1}$ .

It is surprising to note that most of the SDSS QSO systemic redshifts in our sample are blueshifted compared to the nebular  $\text{Ly}\alpha$  emission, and also, most SDSS QSO systemic redshift has large offset with respect to the nebular  $\text{Ly}\alpha$  redshift. Currently, we still do not find a good explanation for such a systematic shift. We only can conclude that with an intrinsic uncertainty of  $300 \text{ km s}^{-1}$  for the empirical calibration of the emission (e.g., Shen et al. 2016), such systemic redshift estimates may not be optimal for our ultraluminous QSO sample. Future efforts are definitely needed to better constrain this fundamental parameter. A better strategy to obtain a more accurate systemic redshift (down to a few tens of  $\text{km s}^{-1}$ ) may require sub-mm observational campaign in future. These sub-mm observations can help us to evaluate whether the systemic redshift derived from Mg II emission is accurate or not for such a high luminosity QSO sample at  $z \approx 2$ .

## 5. SUMMARY

In this paper, we conduct a systematic, blind survey of  $\text{Ly}\alpha$  nebulae around ultraluminous Type-I QSOs at  $z \approx 2$  using the Keck Cosmic Web Imager (KCWI). This survey allows us to directly compare with similar integral-field-spectroscopic studies at  $z \gtrsim 3$  using MUSE and to study the evolution of the cool gas in massive halos. The main conclusion of this paper are as follows:

(1) We find that 14 out of 16 QSOs at  $z \approx 2$  are associated with  $\text{Ly}\alpha$  nebulae with projected linear sizes larger than 50 physical kpc (pkpc). Among them, four nebulae have large  $\text{Ly}\alpha$  emission with surface brightness of  $SB_{\text{Ly}\alpha} > 10^{-17} \text{ erg s}^{-1} \text{ cm}^{-2} \text{ arcsec}^{-2}$  on  $> 100 \text{ kpc}$ , and their scales extend beyond the KCWI field of view.

(2) Our KCWI results suggest that the nebulae at  $z \approx 2$  are one order of magnitude brighter and more extended than previous narrowband surveys indicate (e.g., Arrigoni Battaia et al. 2016). We suggest that this is partially due to the limitation of the narrowband survey technique and a significant fraction of the diffuse  $\text{Ly}\alpha$  emission may have been missed in the narrow-band imaging because of large offsets between the true and the estimated quasar systemic redshift from the MgII line. (see §4.1). The circularly-averaged  $\text{Ly}\alpha$  profile is also much more brighter than that of Lyman break galaxies (LBGs) (e.g., Steidel et al. 2011) and  $\text{Ly}\alpha$  emitters (e.g., Wisotzki et al. 2016). No regular rotational kinematic patterns have been found in the diffuse  $\text{Ly}\alpha$  emission for our QSO sample at  $z \approx 2$ .

(3) We directly measure the circularly-averaged surface brightness (SB) at  $z \approx 2$  using the integral field spectroscopy, and we perform a direct comparison with the  $z \approx 3$  results using VLT/MUSE (Borisova et al. 2016; Arrigoni Battaia et al. 2019). The typical circularly-averaged SB profile of  $\text{Ly}\alpha$  nebulae around  $z \approx 2$  QSOs can be described by a power-law with the slope of  $-1.8$ , same as the one measured for the nebulae around  $z \approx 3$  QSOs, however its normalisation is about a factor 0.4 dex fainter than the SB profiles at  $z \approx 3$ , after correcting for the different redshift dimming. A larger FoV could further constrain the profile on a larger radii, especially to differentiate the exponential and power-law profiles (e.g., Arrigoni Battaia et al. 2019).

(4) Our analysis suggests that the  $\text{Ly}\alpha$  emitting cool gas in the QSO halos at  $z \approx 2$  may have smaller cover fraction (see §4.2). This may be one of the reasons for the lower circularly average SB from  $z \approx 3$  to  $z \approx 2$ . Further, nebulae around  $z \approx 2$  QSOs appear to have more irregular and asymmetric morphologies compared to QSO nebulae at  $z \approx 3$  as quantified by the ratio between the semiminor and semimajor axis above the  $2\sigma$  detection level (and denoted by  $\alpha$  as in Arrigoni Battaia et al. 2019). In particular, the average  $\alpha$  at  $z \approx 2$  is  $\sim 40\%$  smaller than that at  $z \approx 3$ . Taking into account these different morphologies, the local SB values of the  $\text{Ly}\alpha$  region, once corrected for redshift-dimming, become similar between the different redshifts, especially at the radii  $> 60 \text{ kpc}$  (see e.g., Figure 15).

Taken all together, our KCWI results suggest that from  $z \approx 3$  to  $z \approx 2$ , the covering factor and possibly the overall mass of cool  $\text{Ly}\alpha$  emitting CGM could decrease, assuming the same opening angle at  $z \approx 2$  and  $z \approx 3$ . For the  $\text{Ly}\alpha$  emitting region, the typical densities of the cool gas around QSOs do not strongly evolve from  $z \approx 3$  to  $z \approx 2$ . Last but not least, we note that there is still a large scatter and variation in the  $\text{Ly}\alpha$  surface brightness and covering factor among individual systems and that a larger sample would be necessary in order to obtain a better statistical analysis and comparison among different redshifts and QSO properties.

**Acknowledgement:** We acknowledge the discussion of the data reduction and analysis with Chris Martin, Matt Matuszewski, James D. Neill, Erika Hamden, and Donal Sullivan. ZC acknowledges the supports provided by NASA through the Hubble Fellowship grant HST-HF2-51370 awarded by the Space Telescope Science Institute, which is operated by the Association of Universities for Research in Astronomy, Inc., for NASA, under contract NAS 5-26555. SC gratefully acknowledges support from Swiss National Science Foundation grant PP00P2.163824.

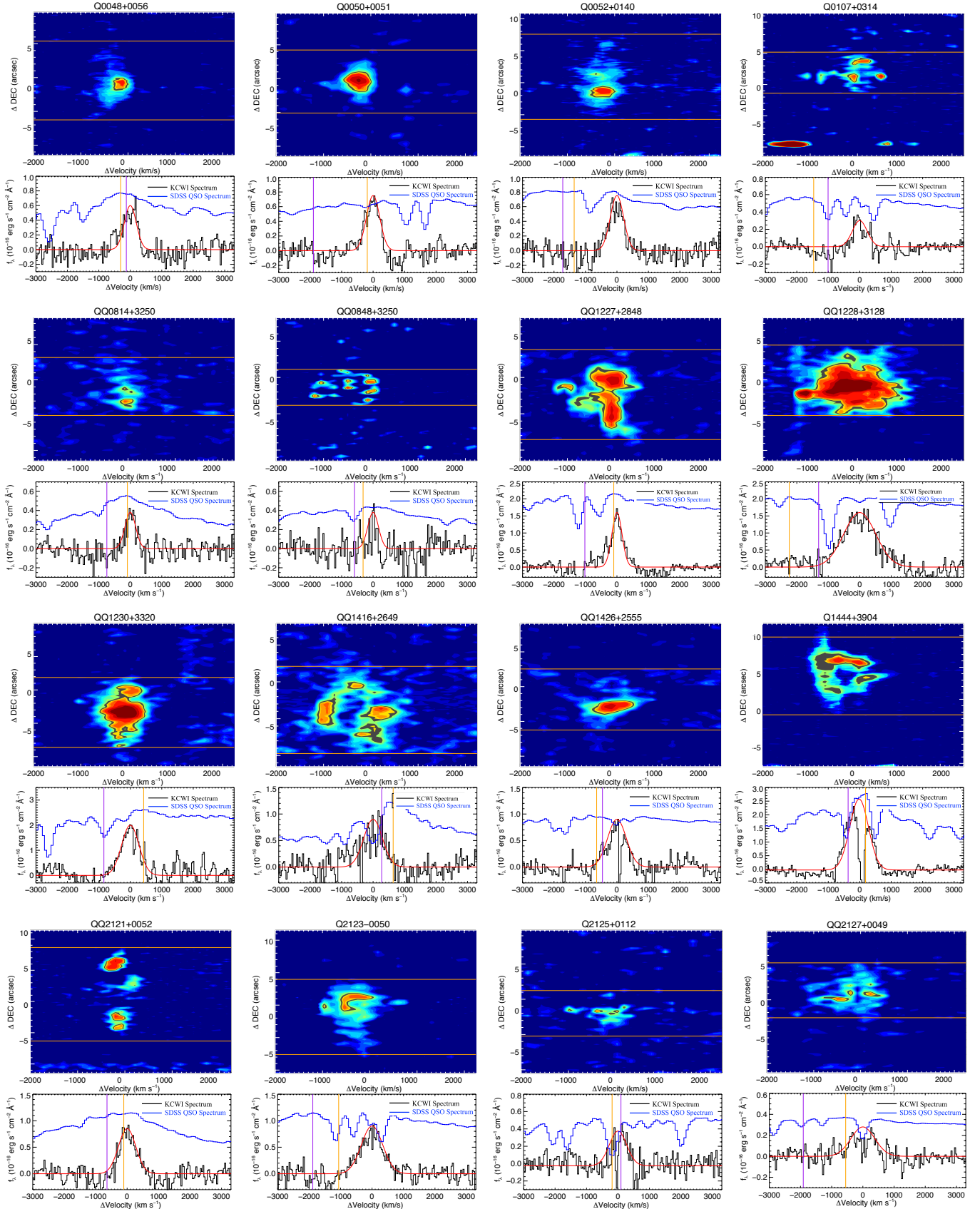


FIG. 7.— The 2-D and 1-D spectra of  $\text{Ly}\alpha$  nebulae at  $z \approx 2$  obtained from KCWI datacubes for each ultraluminous QSO. The upper panel shows the 2-D spectra, extracted using the pseudo-aperture defined by the thick white contours defined in Figure 3 and integrating along the spatial x-axis direction. The lower panels show the 1-D spectra of the nebulae (black lines) obtained by integrating the 1-D spectra along the spatial direction between two horizontal orange lines in the upper panel. We overlay the one-dimensional spectrum of the QSO. Most of radio-quiet nebulae show a  $\text{Ly}\alpha$  spectral shape (black) very different from that of the QSO (blue), confirming that the detected emission is not an artifact of the QSO PSF subtraction. We overplot as a vertical purple line the expected  $\text{Ly}\alpha$  velocity from the systemic redshift of the QSO as determined by the SDSS pipeline fitting routine (Pâris et al. 2017, also see Table 1). The orange vertical line shows instead the systemic redshift obtained by a fit of the quasar broad  $\text{Ly}\alpha$  line.

## REFERENCES

- Alexander, D. M., Swinbank, A. M., Smail, I., McDermid, R., & Nesvadba, N. P. H. 2010, *MNRAS*, 402, 2211
- Arrigoni Battaia, F., Yang, Y., Hennawi, J. F., et al. 2015, *ApJ*, 804, 26
- Arrigoni Battaia, F., Hennawi, J. F., Prochaska, J. X., & Cantalupo, S. 2015, *ApJ*, 809, 163
- Arrigoni Battaia, F., Hennawi, J. F., Cantalupo, S., & Prochaska, J. X. 2016, *ApJ*, 829, 3
- Arrigoni Battaia, F., Prochaska, J. X., Hennawi, J. F., et al. 2018, *MNRAS*, 473, 3907
- Arrigoni Battaia, F., Hennawi, J. F., Prochaska, J. X., et al. 2019, *MNRAS*, 482, 3162
- Bond, J. R., Kofman, L., & Pogosyan, D. 1996, *Nature*, 380, 603
- Borisova, E., Cantalupo, S., Lilly, S. J., et al. 2016, *ApJ*, 831, 39
- Cai, Z., Fan, X., Peirani, S., et al. 2016, *ApJ*, 833, 135
- Cai, Z., Fan, X., Yang, Y., et al. 2017, *ApJ*, 837, 71
- Cai, Z., Fan, X., Bian, F., et al. 2017, *ApJ*, 839, 131
- Cai, Z., Hamden, E., Matuszewski, M., et al. 2018, *ApJ*, 861, L3
- Cantalupo, S., Porciani, C., Lilly, S. J., & Miniati, F. 2005, *ApJ*, 628, 61
- Cantalupo, S., Lilly, S. J., & Haehnelt, M. G. 2012, *MNRAS*, 425, 1992
- Cantalupo, S., Arrigoni-Battaia, F., Prochaska, J. X., Hennawi, J. F., & Madau, P. 2014, *Nature*, 506, 63
- Cantalupo, S. 2017, *Gas Accretion onto Galaxies*, 430, 195
- Cantalupo, S., Pezzulli, G., Lilly, S. J., et al. 2019, *MNRAS*, 483, 5188
- Ciardullo, R., Gronwall, C., Wolf, C., et al. 2012, *ApJ*, 744, 110
- Correa, C. A., Wyithe, J. S. B., Schaye, J., & Duffy, A. R. 2015, *MNRAS*, 450, 1521
- Dekel, A., Birnboim, Y., Engel, G., et al. 2009, *Nature*, 457, 451
- Dekel, A., Zolotov, A., Tweed, D., et al. 2013, *MNRAS*, 435, 999
- Dijkstra, M., Haiman, Z., & Spaans, M. 2006, *ApJ*, 649, 37
- Faucher-Giguère, C.-A., Hopkins, P. F., Kereš, D., et al. 2015, *MNRAS*, 449, 987
- Fukugita, M., Hogan, C. J., & Peebles, P. J. E. 1998, *ApJ*, 503, 518
- Fumagalli, M., O’Meara, J. M., & Prochaska, J. X. 2011, *Science*, 334, 1245
- Fumagalli, M., Hennawi, J. F., Prochaska, J. X., et al. 2014, *ApJ*, 780, 74
- Gould, A., & Weinberg, D. H. 1996, *ApJ*, 468, 462
- Herenz, E. C., Wisotzki, L., Roth, M., & Anders, F. 2015, *A&A*, 576, A115
- Hogan, C. J., & Weymann, R. J. 1987, *MNRAS*, 225, 1P
- Kennicutt, R. C., & Evans, N. J. 2012, *ARA&A*, 50, 531
- Kereš, D., Katz, N., Weinberg, D. H., & Davé, R. 2005, *MNRAS*, 363, 2
- Kereš, D., Katz, N., Fardal, M., Davé, R., & Weinberg, D. H. 2009, *MNRAS*, 395, 160
- Kollmeier, J. A., Zheng, Z., Davé, R., et al. 2010, *ApJ*, 708, 1048
- Lau, M. W., Prochaska, J. X., & Hennawi, J. F. 2016, *ApJS*, 226, 25
- Leibler, C. N., Cantalupo, S., Holden, B. P., & Madau, P. 2018, *MNRAS*, 480, 2094
- Lusso, E., Worseck, G., Hennawi, J. F., et al. 2015, *MNRAS*, 449, 4204
- Harrison, C. M., Alexander, D. M., Mullaney, J. R., & Swinbank, A. M. 2014, *MNRAS*, 441, 3306
- Hennawi, J. F., & Prochaska, J. X. 2013, *ApJ*, 766, 58
- Hennawi, J. F., Prochaska, J. X., Cantalupo, S., & Arrigoni-Battaia, F. 2015, *Science*, 348, 779
- Ji, S., Peng Oh, S., & McCourt, M. 2018, *MNRAS*,
- Martin, D. C., Chang, D., Matuszewski, M., et al. 2014, *ApJ*, 786, 106
- Martin, D. C., Matuszewski, M., Morrissey, P., et al. 2015, *Nature*, 524, 192
- Marino, R. A., Cantalupo, S., Pezzulli, G., et al. 2019, *arXiv e-prints*, arXiv:1906.06347
- McQuinn, M. 2016, *ARA&A*, 54, 313
- Morrissey, P., Matuszewski, M., Martin, D. C., et al. 2018, *ApJ*, 864, 93
- Nelson, D., Vogelsberger, M., Genel, S., et al. 2013, *MNRAS*, 429, 3353
- Oklopčić, A., Hopkins, P. F., Feldmann, R., et al. 2017, *MNRAS*, 465, 952
- Onoue, M., Kashikawa, N., Uchiyama, H., et al. 2018, *PASJ*, 70, S31
- Pâris, I., Petitjean, P., Aubourg, E., et al. 2017, *arXiv:1712.05029*
- Prescott, M. K. M., Dey, A., & Jannuzi, B. T. 2009, *ApJ*, 702, 554
- Shen, Y., Strauss, M. A., Oguri, M., et al. 2007, *AJ*, 133, 2222
- Shen, S., Madau, P., Guedes, J., et al. 2013, *ApJ*, 765, 89
- Steidel, C. C., Bogosavljević, M., Shapley, A. E., et al. 2011, *ApJ*, 736, 160
- Stewart, K. R., Kaufmann, T., Bullock, J. S., et al. 2011, *ApJ*, 735, L1
- Stewart, K. R., Brooks, A. M., Bullock, J. S., et al. 2013, *ApJ*, 769, 74
- Trainor, R. F., Strom, A. L., Steidel, C. C., & Rudie, G. C. 2016, *ApJ*, 832, 171
- Valentino, F., Daddi, E., Finoguenov, A., et al. 2016, *ApJ*, 829, 53
- van de Voort, F., Schaye, J., Booth, C. M., Haas, M. R., & Dalla Vecchia, C. 2011, *MNRAS*, 414, 2458
- Villar-Martín, M., Sánchez, S. F., Humphrey, A., et al. 2007, *MNRAS*, 378, 416
- Vogelsberger, M., Genel, S., Sijacki, D., et al. 2013, *MNRAS*, 436, 3031
- White, M., Myers, A. D., Ross, N. P., et al. 2012, *MNRAS*, 424, 933
- Wisotzki, L., Bacon, R., Blaizot, J., et al. 2016, *A&A*, 587, A98
- Yang, Y., Zabludoff, A., Jahnke, K., & Davé, R. 2014, *ApJ*, 793, 114



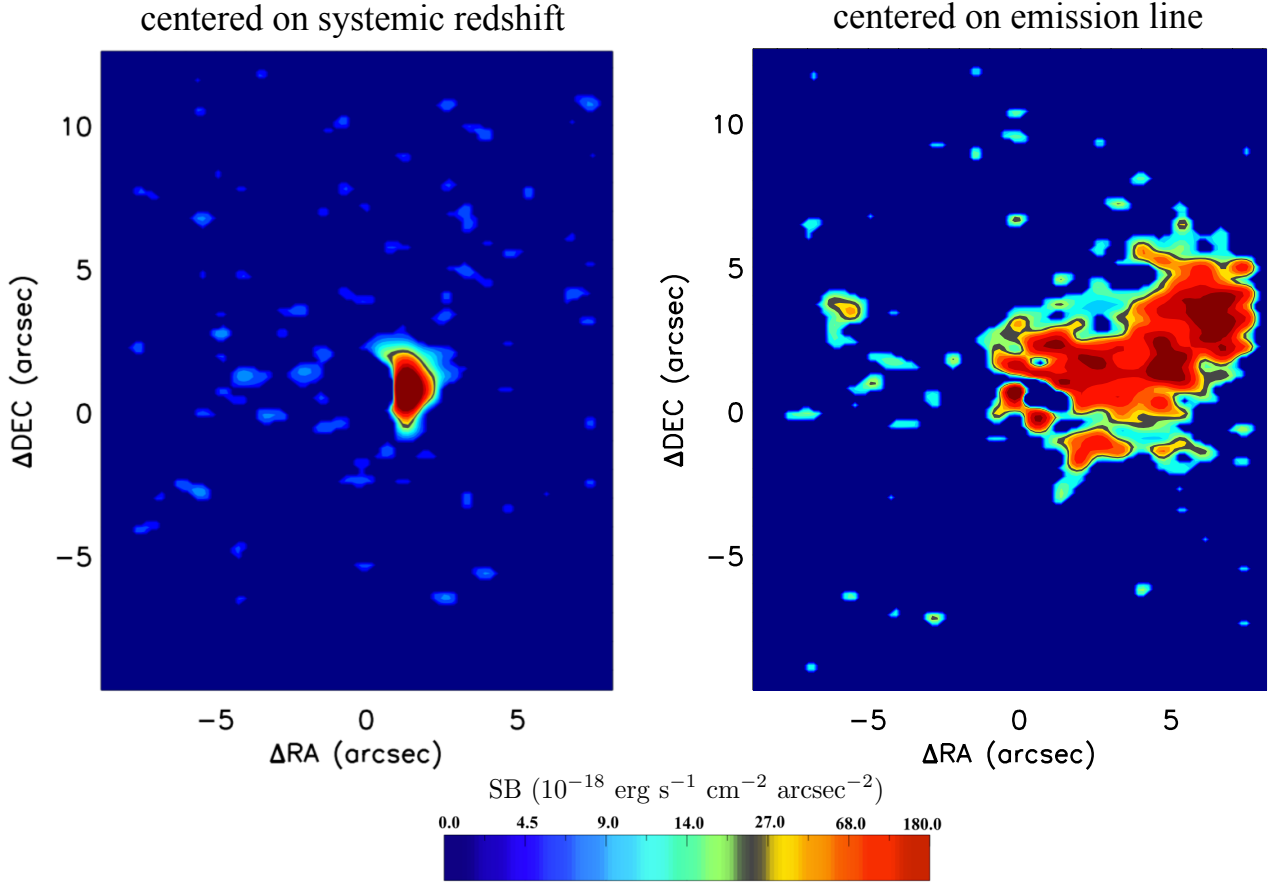


FIG. 8.— Comparison between two pseudo-narrowband images of Q1228 obtained with different filter central wavelengths. The left panel shows a pseudo-narrow band image obtained assuming as the filter central wavelength the systemic redshift determined using the MgII emission (Table 1). The right image uses instead the nebula Ly $\alpha$  redshift as the filter central wavelength. The narrowband we use has a similar profile of NB3950 (e.g., Cantalupo et al. 2014), and the surface brightness is calculated by integrating the flux over a wavelength bin of 30 Å.

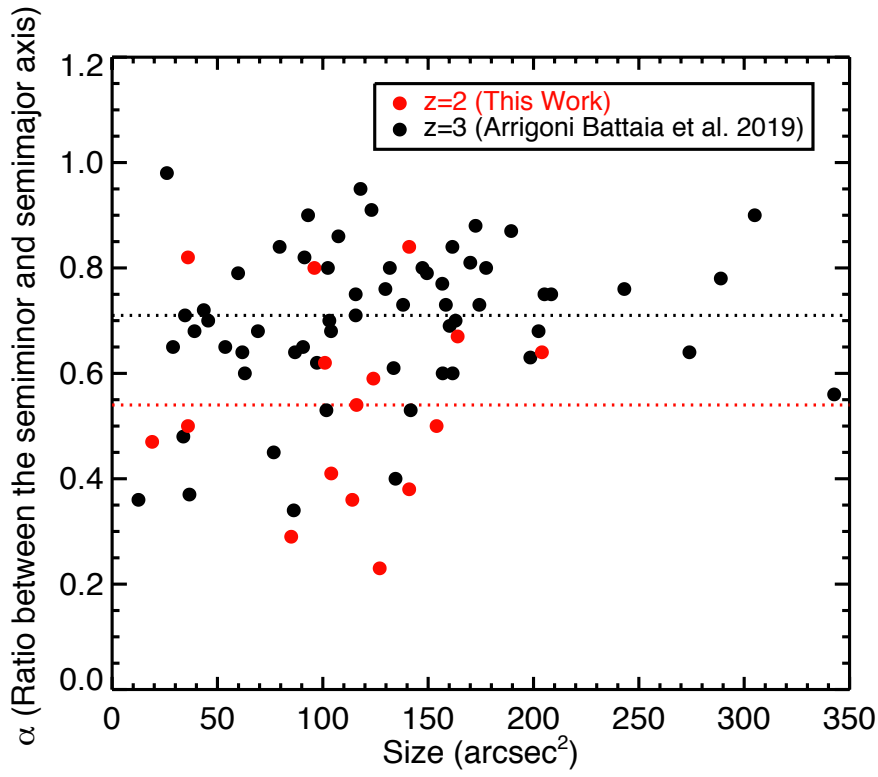


FIG. 9.— Plot of the asymmetry  $\alpha$ , i.e. the ratio between the semiminor axis  $b$  and semimajor axis  $a$ , versus the area enclosed by the  $2\sigma$  isophote. Black indicates the QSOs in Arrigoni Battaia et al. (2019) at  $z \approx 3.1$ ; and the red represents QSOs in our sample at  $z \approx 2.2$ . Our sample has a median  $\alpha$  value of 0.54 (red horizontal dotted line), comparing with the median  $\alpha$  of 0.71 at  $z \approx 3$  (black horizontal dotted line). Although a larger sample is needed, our current data tentatively suggests that the QSOs at  $z \approx 2$  could be more asymmetric than that at  $z \approx 3$ .

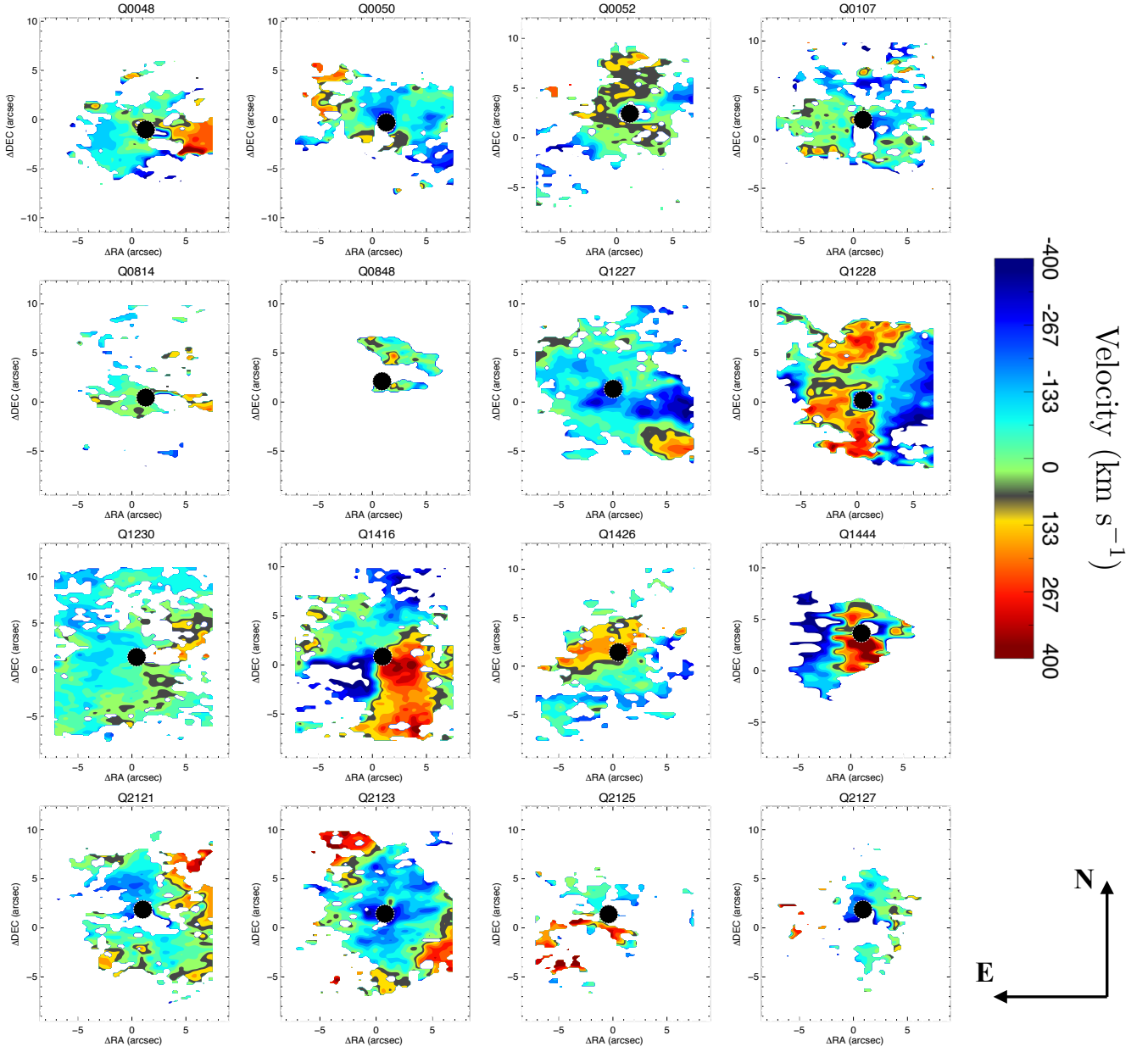


FIG. 10.— This figure shows the flux-weighted velocity map for individual QSOs at  $z \approx 2$  using KCWI.

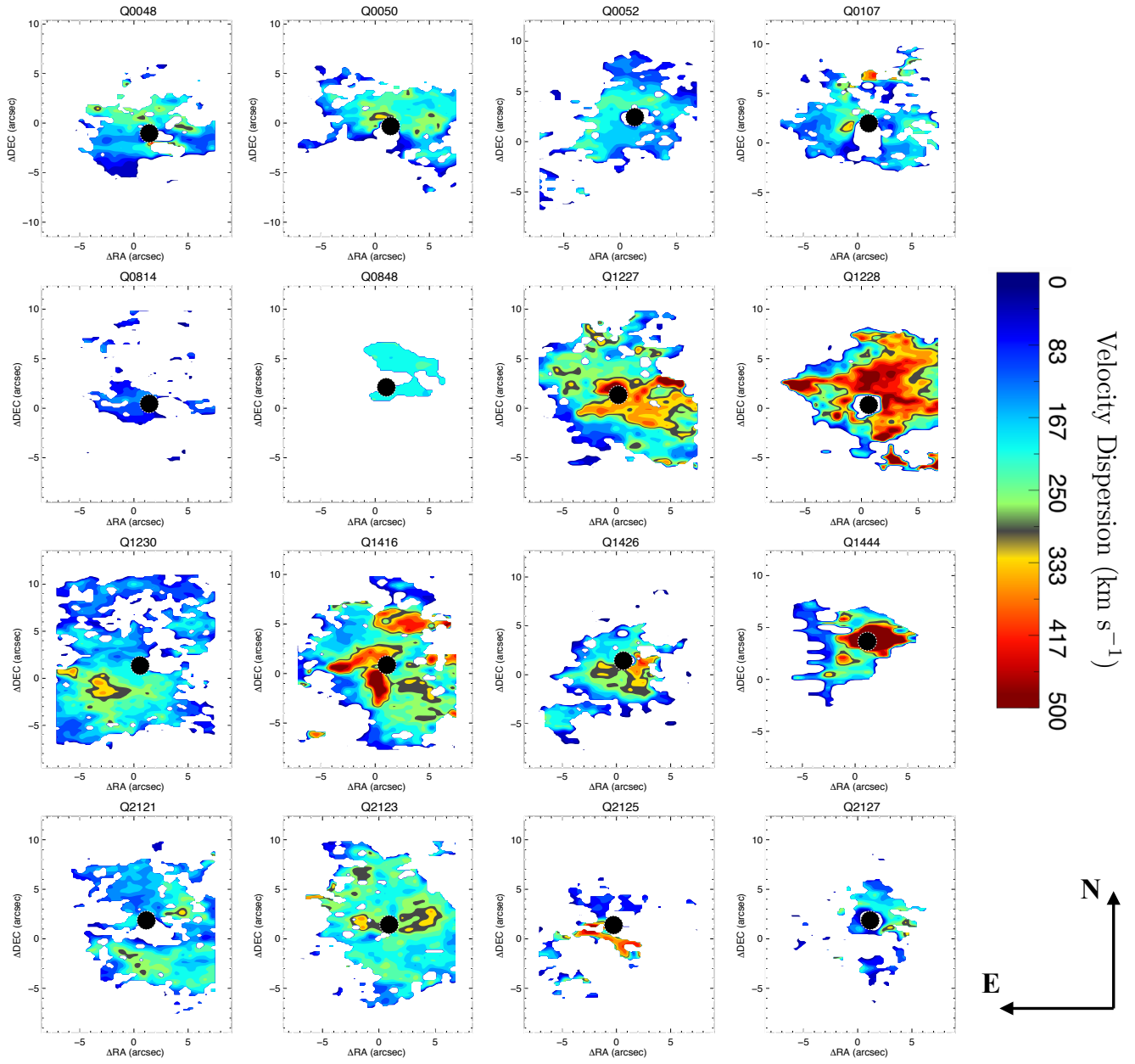


FIG. 11.— This figure shows the flux-weighted velocity dispersion map for individual QSOs at  $z \approx 2$  using KCWI.

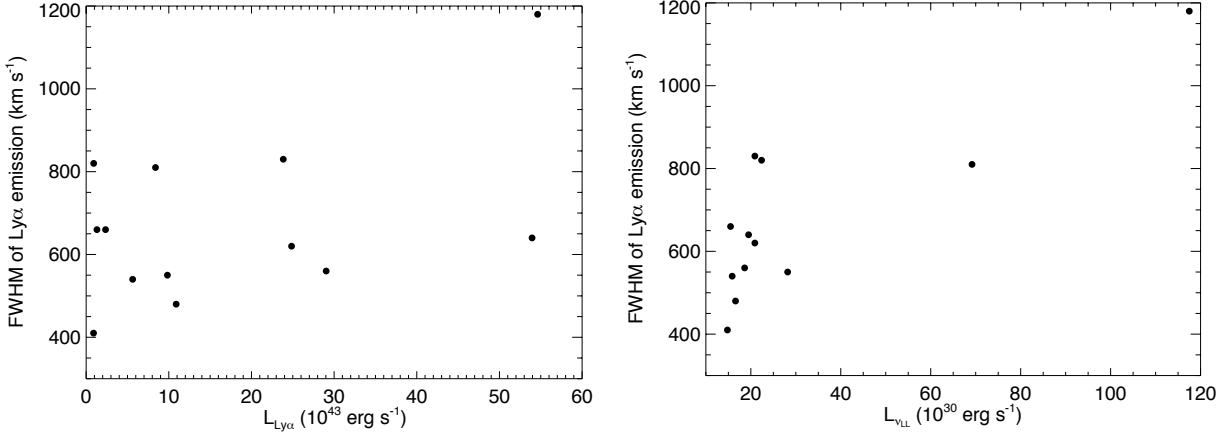


FIG. 12.— The left panel shows that the FWHM of Ly $\alpha$  emission as a function of nebular Ly $\alpha$  luminosity. The right panel indicates the size of the FWHM of Ly $\alpha$  emission as a function of ionization luminosity. Due to the extremely high SNR of Ly $\alpha$  emission, the luminosity measurement has a typical error of  $\leq 1\%$  and the FWHM measurement has a typical error of 10% (see Table 1). No strong correlation between the FWHM and the nebular Ly $\alpha$  luminosity is found.

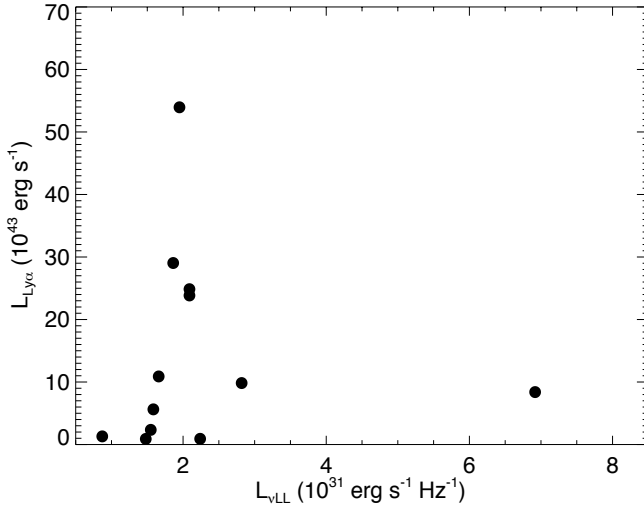


FIG. 13.— The relation between the Ly $\alpha$  luminosity and the QSO ionizing flux  $L_{\nu_{\text{LL}}}$ . From this figure, we can see that there is no obvious correlation between  $L_{\text{Ly}\alpha}$  and  $L_{\nu_{\text{LL}}}$ , suggesting the nebular powering mechanism cannot be dominated by optically thick photoionization scenario. The typical statistical error of the data points in this figure is less than 1% (see Table 1).

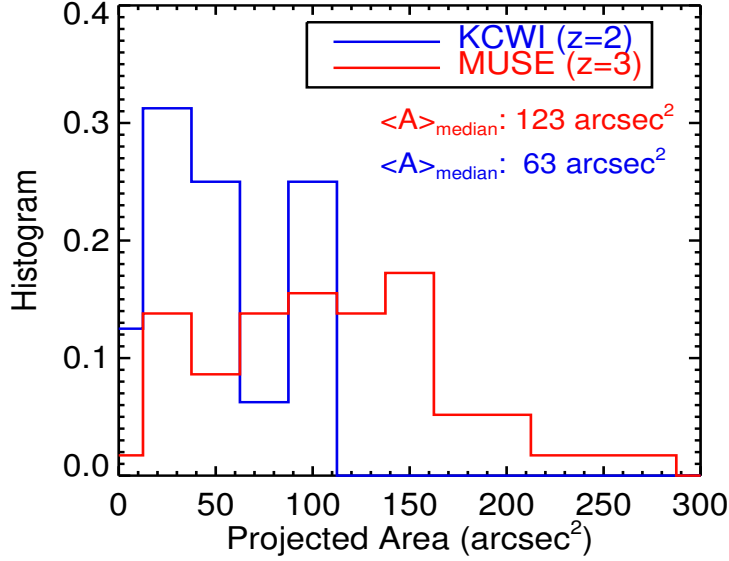


FIG. 14.— The distribution of the projected area with redshifted surface brightness ( $SB_{z=2.3}$ ) greater than  $1.0 \times 10^{-17} \text{ erg s}^{-1} \text{ cm}^{-2} \text{ arcsec}^{-2}$ . Because all MUSE nebulae at  $z \approx 3$  have redshifted  $SB_{z=2.3} \gtrsim 1.0 \times 10^{-17} \text{ erg s}^{-1} \text{ cm}^{-2} \text{ arcsec}^{-2}$  contour smaller than the KCWI FoV ( $16'' \times 20''$ ), the area at  $z \approx 2$  and  $z \approx 3$  can be directly compared without correcting the difference of the FoVs between KCWI and MUSE. The median projected area at  $z = 2.3$  is  $63 \text{ arcsec}^2$  which is about 51.3% of the median area of  $A_{\text{median}} = 123 \text{ arcsec}^2$  for nebulae at  $z \approx 3.1$ .

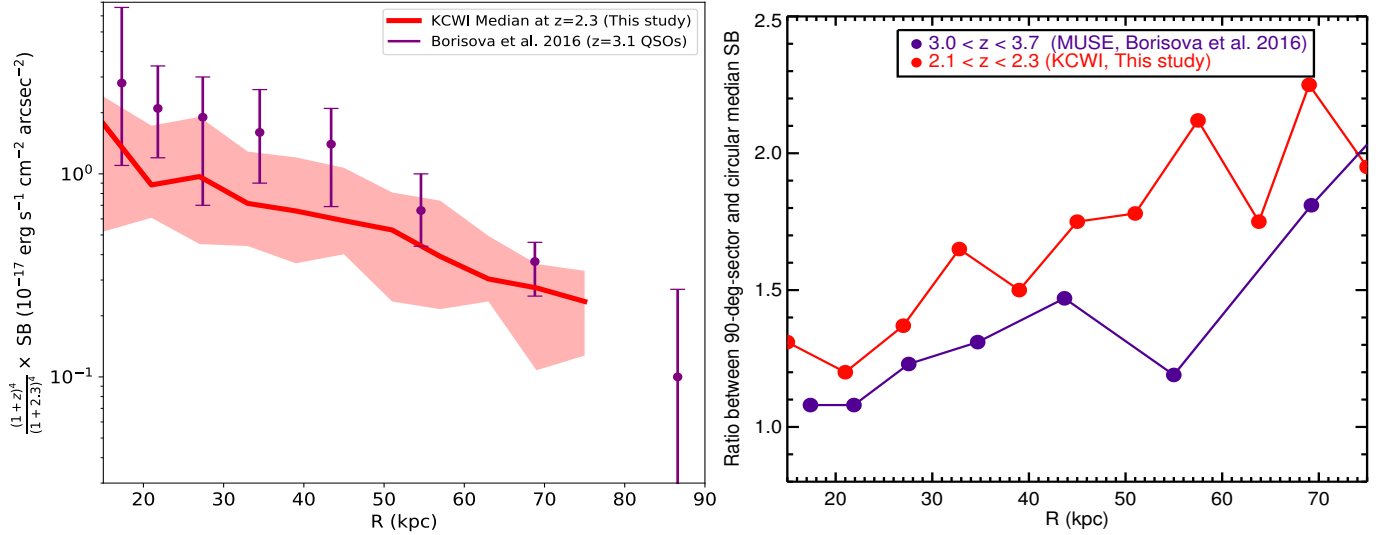


FIG. 15.— *Left*: SB profiles averaged over a 90-degree quadrant chosen as the one with the highest flux. *Right*: the ratio between the SB in 90-degree-sectors and the median SB in full annuli. On 15 – 70 kpc, the ratio at  $z \approx 2.3$  (red) is higher than that at  $z \approx 3$  (purple), suggesting that the covering factor of the Ly $\alpha$  emitting clouds at  $z \approx 2$  is smaller than  $z \approx 3$  in these two samples.

TABLE 1  
QSO PROPERTIES AT  $z \approx 2$  IN OUR QSO SNAPSHOT PROGRAM

Name	RA	DEC	$z_{\text{Ly}\alpha}^{(a)}$	$z_{\text{pipe}}$	$z_{\text{PCA}}$	$z_{\text{MgII}}$	$i\text{-mag}^{(b)}$	$\text{Log}_{10} L_{\text{PLL}}^{(c)}$	$L_{\text{Ly}\alpha}$ ( $10^{43} \text{ erg s}^{-1}$ )	$\text{FWHM}_{\text{Ly}\alpha}$ ( $\text{km s}^{-1}$ )	Projected Extent (kpc)	$2\sigma_{\text{SB}}^{(d)}$ $\text{cgs}(\text{g})$	Seeing (arcsec)	Asymmetry $\alpha$
Q0048+0056	00:48:56.34	+00:56:48.1	2.328	2.327	2.323	2.327	17.99±0.01	31.20	2.28	542 ± 28	104	1.8	0.9''	0.50
Q0050+0051	00:50:21.22	+00:51:35.0	2.241	2.220	2.219	2.222	17.82±0.01	31.22	2.00	481 ± 29	116	1.8	0.9''	0.59
Q0052+0140	00:52:33.67	+01:40:40.8	2.309	2.291	2.302	2.300	17.34±0.01	31.45	2.03	549 ± 29	127	1.7	0.8''	0.61
Q0107+0314	01:07:36.90	+03:14:59.2	2.280	2.269	2.264	2.262	18.01±0.01	31.17	1.52	410 ± 30	114	1.8	0.9''	0.51
Q0814+3250	08:14:01.38	+32:50:48.1	2.219	2.211	2.223	2.222	18.50±0.01	30.94	0.15	662 ± 32	85	1.7	0.8''	0.31
Q0848-0114 <sup>(e)</sup>	08:48:56.95	-01:14:58.9	2.300	2.293	2.301	2.302	18.40±0.01	30.91	0.13	378 ± 21	28	2.3	1.1''	0.50
Q1227+2848	12:27:27.48	+28:48:47.9	2.265	2.255	2.266	2.268	17.73±0.01	31.27	5.77	557 ± 31	> 164	1.8	0.9''	0.36
Q1228+3128	12:28:24.97	+31:28:37.7	2.214	2.220	2.199	2.231	15.68±0.01	32.07	12.29	1175 ± 39	> 124	1.9	0.9''	0.52
Q1230+3320	12:30:35.47	+33:20:00.5	2.323	2.314	2.309	2.313	17.76±0.01	31.29	12.40	643 ± 22	> 204	2.0	1.0''	0.73
Q1416+2649	14:16:17.38	+26:49:06.2	2.293	2.296	2.340	2.301	18.04±0.01	31.16	5.00	829 ± 32	> 141	2.1	1.1''	0.52
Q1426+2555	14:26:35.86	+25:55:23.7	2.255	2.248	2.249	2.256	17.60±0.01	31.32	3.88	622 ± 26	96	1.9	0.9''	0.84
Q1444+3904	14:44:55.89	+39:04:00.7	2.250	2.250	2.251	2.250	18.40±0.01	31.26	10.09	951 ± 40	101	2.1	1.1''	0.70
Q2121+0052	21:21:59.04	+00:52:24.1	2.373	2.367	2.372	2.377	18.07±0.01	31.19	4.56	656 ± 32	> 141	1.8	0.8''	0.38
Q2123-0050	21:23:29.46	-00:50:52.9	2.280	2.250	2.266	2.271	16.34±0.01	31.84	3.59	812 ± 35	> 154	2.0	1.0''	0.50
Q2125+0112 <sup>(f)</sup>	21:25:11.83	+01:12:22.32	2.199	2.200	2.202	2.203	18.51±0.01	31.01	1.29	514 ± 60	19	2.3	1.1''	0.60
Q2127+0049	21:27:47.43	+00:49:29.5	2.269	2.245	2.251	2.261	17.53±0.01	31.35	1.10	820 ± 41	58	1.8	0.9''	0.69

(a): The Ly $\alpha$  emission has an extremely high SNR, yielding the typical uncertainties of the Ly $\alpha$  line center of 0.02 Å,

corresponding to the statistical error of Ly $\alpha$  redshift of  $\lesssim 0.001$ .

(b): The  $i$ -magnitude error of these sources have a typical error of  $i$ -magnitude  $\leq 0.01$ . The magnitude are taken from the SDSS Data Release 12.

(c): The ionizing luminosity of the QSO is determined by rescaling the composite spectrum from Lusso et al. (2015) to the QSO luminosity

at the rest-frame 1350 Å. The typical statistical error is  $\leq 1\%$  level.

(d): The surface brightness uncertainty is calculated by integrating over 1 Å at around  $\lambda \approx 1230\text{Å}$ , between Ly $\alpha$  and NV emission, using circles with 1'' diameter.

(e): Q0848-0114 was taken under a partially thin cloudy condition.

(f): Q2125+0112 was taken under a partially thin cloudy condition.

(g):  $\text{cgs}: 10^{-18} \text{ erg s}^{-1} \text{ cm}^{-2} \text{ arcsec}^{-2}$